TECHNICAL
UNIVERSITY OF CRETE
SCHOOL OF PRODUCTION
ENGINEERING AND MANAGEMENT

MODELING AND CONTROL OF A PEM FUEL CELL FOR USE IN HYDROGEN VEHICLES

Thesis by:

CHARALAMPOUS NIKOLAOS

Thesis Advisor:

IPSAKIS DIMITRIOS

Members of the Examination Committee:

Dr. Doitsidis Lefteris

Savvas Piperidis

Chania, 2025

ABSTRACT

This thesis focuses on the dynamic modeling and control of a Proton Exchange Membrane (PEM) fuel cell stack intended for hydrogen-powered vehicle applications. PEM fuel cells are increasingly important in clean energy technologies due to their high efficiency, low emissions, and rapid dynamic response. The accurate modeling and design of appropriate control strategies are thus critical to optimizing their performance and integration into energy systems.

The system is first modeled using a set of nonlinear differential equations, which describe the core state variables of the fuel cell stack, including chemical concentrations, thermal dynamics, current production, and reactant flows. This nonlinear model is then linearized using a Taylor series expansion around steady-state points, resulting in a simplified linear form. Subsequently, the model is expressed in state-space representation, enabling the application of advanced control methodologies.

Following model development, simulation results are presented for each of the three models—nonlinear, linear, and state-space. These models are compared under nominal and perturbed conditions by introducing ±30% changes in hydrogen input flow and coolant mass flow rate (air). The consistency of the results confirms the equivalence and accuracy of the state-space model, making it suitable for control design.

In the final phase, two closed-loop control problems are addressed: regulating the output current through hydrogen input and managing system temperature via coolant flow. Controllers of type P, PI, and PID are designed using the Ziegler–Nichols and Tyreus–Luyben tuning methods. Their performance is assessed using standard performance criteria (ISE, IAE, ITSE, IATE). Simulation results indicate that the PID controller tuned via Tyreus–Luyben performs best for current control, while the Ziegler–Nichols PID configuration is more effective for temperature regulation.

ΠΕΡΙΛΗΨΗ

Η παρούσα διπλωματική εργασία επικεντρώνεται στη μοντελοποίηση και στον έλεγχο μιας στοίβας κυψελών καυσίμου τύπου PEM (Proton Exchange Membrane), με σκοπό τη χρήση της σε συστήματα υδρογονοκίνητων οχημάτων. Οι κυψέλες καυσίμου τύπου PEM παρουσιάζουν ιδιαίτερο ενδιαφέρον λόγω της υψηλής ενεργειακής τους απόδοσης, της χαμηλής εκπομπής ρύπων και της γρήγορης απόκρισης σε δυναμικές απαιτήσεις φορτίου. Για τον λόγο αυτό, η ακριβής περιγραφή της λειτουργίας τους και η ανάπτυξη κατάλληλων ελεγκτών αποτελούν ουσιαστικά βήματα προς την αποτελεσματική ενσωμάτωσή τους σε σύγχρονες ενεργειακές εφαρμογές.

Η μοντελοποίηση του συστήματος πραγματοποιείται αρχικά μέσω μη γραμμικών διαφορικών εξισώσεων, οι οποίες περιγράφουν τις κύριες μεταβλητές κατάστασης και τα φυσικοχημικά φαινόμενα που λαμβάνουν χώρα εντός του συστήματος της στοίβας κυψελών καυσίμου. Περιλαμβάνονται μεταβολές στις συγκεντρώσεις των αερίων συστατικών, θερμικές μεταβολές, ηλεκτρική ισχύς, ηλεκτροχημικές απώλειες και ροές εισόδου/εξόδου. Ακολουθεί η διαδικασία της γραμμικοποίησης του μοντέλου με χρήση της σειράς Taylor, γύρω από προκαθορισμένα σημεία ισορροπίας. Το αποτέλεσμα είναι ένα γραμμικό μοντέλο, το οποίο στη συνέχεια μετατρέπεται σε μοντέλο χώρου-κατάστασης, επιτρέποντας την ευκολότερη εφαρμογή τεχνικών ελέγχου και ανάλυσης (δηλ. με χρήση συναρτήσεων μεταφοράς). Στο δεύτερο στάδιο, πραγματοποιείται η σύγκριση των τριών μοντέλων (μη γραμμικό, γραμμικό, χώρου-κατάστασης. Εξετάζονται διαφορετικές αρχικές συνθήκες και πραγματοποιούνται προσομοιώσεις για μεταβολές ±30% στην παροχή υδρογόνου και στη ροή του ψυκτικού μέσου(αέρας). Τα αποτελέσματα παρουσιάζονται σε μορφή γραφικών παραστάσεων και αναλύονται με στόχο την επαλήθευση της δυναμικής και στατικής ομοιότητας μεταξύ των μοντέλων. Το σύνολο αυτής της ανάλυσης αποδεικνύει την ακρίβεια και τη χρησιμότητα του μοντέλου χώρου-κατάστασης ως μέσο εφαρμογής ελέγχου.

Στο τρίτο μέρος της εργασίας εξετάζεται η διαδικασία ελέγχου μέσω της ανάπτυξης ελεγκτών κλειστού βρόχου. Αρχικά παρουσιάζεται η θεωρία των συστημάτων αυτομάτου ελέγχου, δίνοντας έμφαση στον καθορισμό της ευστάθειας μέσω της τοπολογίας των πόλων (root locus) και στην εύρεση κρίσιμων παραμέτρων, όπως το κρίσιμο κέρδος Kcr και η κρίσιμη περίοδος Pcr. Με βάση τις τιμές αυτές εφαρμόζονται οι μέθοδοι Ziegler-Nichols και Tyreus–Luyben για τη ρύθμιση ελεγκτών τύπου P, PI και PID.

Οι ελεγκτές αξιολογούνται μέσω της προσομοίωσης της επίδρασής τους σε δύο βασικά υποσυστήματα: (1) τον έλεγχο του παραγόμενου ρεύματος εξόδου μέσω της ροής υδρογόνου και (2) τον έλεγχο της θερμοκρασίας εξόδου μέσω της ροής του ψυκτικού μέσου . Οι αποδόσεις των ελεγκτών συγκρίνονται με τη χρήση ποσοτικών δεικτών επίδοσης (ISE, IAE, ITSE, IATE), οδηγώντας στην εξαγωγή συμπερασμάτων σχετικά με την αποτελεσματικότητα κάθε μεθόδου. Από την ανάλυση προκύπτει ότι για τον έλεγχο του ρεύματος ο πιο αποδοτικός ελεγκτής είναι ο PID που ρυθμίστηκε με τη μέθοδο Tyreus–Luyben, ενώ για την θερμοκρασία η καλύτερη συμπεριφορά παρατηρείται στον PID της μεθόδου Ziegler-Nichols.

Συνολικά, η παρούσα εργασία καταδεικνύει την αναγκαιότητα της μοντελοποίησης με ακρίβεια και της επιλογής κατάλληλων ελεγκτών για τη βελτιστοποίηση της λειτουργίας μιας κυψέλης καυσίμου τύπου PEM, ενισχύοντας την αξιοπιστία της ως πηγή ενέργειας για εφαρμογές κινητικότητας.

ACKNOWLEDGEMENTS

At the beginning of this thesis, I would like to express my sincere gratitude to **Assistant Professor Dimitris Ipsakis**, supervisor of this project, for his invaluable support, guidance, and insightful knowledge throughout the entire course of this work. His consistent encouragement and the creative academic environment he fostered were instrumental in the successful completion of this study.

I would also like to thank the **student research team TUCER** and its coordinator, **Mr. Savvas Piperidis**, for providing critical technical data regarding the operation of the fuel cell used in this research.

Finally, I am deeply grateful to my **family** for their unwavering support throughout my academic journey, as well as to all **friends and fellow students** who, through their guidance, encouragement, and assistance in every aspect, helped me successfully complete this important and memorable chapter of my life.

TABLE OF CONTENTS

Chapter 1: MATHEMATICAL MODELLING OF THE PEM FUEL CELL

Chapter introduction

The mathematical modelling of dynamic systems is a procedure that involves the development of mathematical equations that will describe the main features of the PEM Fuel Cell stack operation. It is highlighted that these features should include the multiple phenomena taking place and evolve through time (dynamics). It is also important, that the proposed model will be able to be verified (model validation) from experimental data (if available).

Following this analysis, the mathematical modelling of the PEM fuel cell is carried out using ordinary differential equations (ODEs). The equations describe the behavior of physical quantities on the time scale, at the exit of the fuel cell and have been solved with MATLAB.

It is noted that in many cases of describing mechanical devices with differential equations, the solution proves to be difficult or even impossible due to their non-linear nature. In cases where the model is non-linear it is necessary to linearize it so that to enable its solution. For the linearization of the model, the Taylor series approach was used.:

$x(t_s) = x_s$, which is called the steady state point and the derivative at it is

$\frac{dx(t_s)}{dt} = 0$.

Furthermore, as soon as the linear model is verified, the identical state-space model will be provided in the following sections.

1.1 Dynamic modelling of the PEM fuel cell

The operation of a fuel cell depends on the amount of fuel input, i.e. hydrogen at the anode inlet and oxygen/nitrogen (air) at the cathode inlet, which affects both the operating temperature and the efficiency of the power output. At the same time, thanks to the electrochemical reactions that takes place inside the cell (electrolysis), water is also produced which exits from the cathode outlet. Afterwards, all the necessary mathematical relations will be given in detail, both differential and non-differential, describing how the process works in real terms conditions.

The first modelling phase for the description of the fuel cell's operation includes the development of non-linear differential equations.

The anode/cathode volumetric flowrate and inlet concertation are given as:

- $Q_{in\_anode} = (F_{in\_fc\_an} * Rg * T_{in\_fc})/(P_{fc})$ **(1.1)**
- $Q_{out\_anode} = (F_{out\_fc\_an} * Rg * T_{out\_fc})/(P_{fc})$ **(1.2)**
- $C_{in\_fc\_hydrogen} = F_{in\_fc\_hydrogen}/Q_{in\_anode}$ **(1.3)**

- $Q_{in\_cathode} = (F_{in\_fc\_cat} * Rg * T_{in\_fc})/(P_{fc})$ **(1.4)**
- $Q_{out\_cathode\_gas} = (F_{out\_fc\_cat\_gas} * Rg * T_{out\_fc})/(P_{fc})$ **(1.5)**
- $Q_{out\_cathode\_liquid} = (F_{out\_fc\_cat\_liquid} * 18 * 10^{-6})$ **(1.6)**

where $F_{in\_fc/F_{out\_fc}}$, refers to the hydrogen inlet and outlet flow in mol/s respectively, Rg stands for the universal gas constant as 8.314 J/mol*K, T_{in}, T_{out} refers to the inlet and outlet temperature in K and P_{fc} is the operating pressure of the system in bar or atm, $F_{out\_fc\_cat\_gas}$, $F_{out\_fc\_cat\_liquid}$ represent the sum of the gas (O_2 and N_2) and liquid (Water) flows present at the cathode side of the system, respectively.

- $C_{in\_fc\_oxygen\_cat} = F_{in\_fc\_oxygen\_cat}/Q_{in\_cathode}$ **(1.7)**
- $C_{in\_fc\_nitrogen\_cat} = F_{in\_fc\_nitrogen\_cat}/Q_{in\_cathode}$ **(1.8)**
- $C_{in\_fc\_water\_cat} = F_{in\_fc\_water\_cat}/Q_{in\_cathode}$ **(1.9)**

where $F_{in\_fc\_{oxygen_{cat}}}/F_{in\_fc\_nitrogen\_cat}$ refers to the oxygen and nitrogen inlet flow in mol/s respectively.

The electrochemical equations will be carried out to explain the relationship between voltage and power:

- $P_{total} = I_{fc} * V_{total}$ **(1.10)**
- $V_{total} = V_{fc} * nc$ **(1.11)**

The operating voltage is described by the Nernst equation:

$$Vfc = Enerst - nact + Vohmic - Vconc\ , \qquad \textbf{(1.12)}$$

where,

- $Enernst$ denotes the thermodynamically permissible voltage (in Volt) of the fuel cell as described by the Nernst equation.

- **Activation losses** $Vact$: These arise due to the sluggish kinetics of electrochemical reactions occurring on the surface of the electrodes. At the initial stage of fuel cell operation, a portion of the open-circuit voltage is consumed to facilitate electron transfer to and from the electrodes.

This phenomenon is analogous to the activation energy required for initiating any chemical reaction.

- **Ohmic losses** *Vohm*: These are attributed to the internal resistance within the system, including the resistance to electron flow between the electrodes and the ionic resistance encountered by ions moving through the electrolyte.

- **Concentration losses** *Vconc*: These result from the gradual depletion in the concentration of the supplied reactant gases, leading to a drop in their partial pressures and subsequently causing a reduction in cell voltage.

❖ $Enerst = 1.229 - (0.85 \cdot 10^{-3}) * (T_{out\_fc} - 298) + (4.3085 \cdot 10^{-5}) * T_{out\_fc} * (log(P_{hydrogen\_anode}) + 0.5 * log(P_{oxygen\_cathode}))$ **(1.13)**

❖ $Vact = x1 + x2 * T_{out\_fc} + x3 * T_{out\_fc} * (log(I_{fc})) + x4 * T_{out\_fc} * log(C_{oxygen\_interface})$ **(1.14)**

❖ $Vohmic = -I_{fc} * Rohm$ **(1.15)**

❖ $Vconc = -(Rg * T_{out\_fc}/(ne * Far)) * log(1 - (I_{fc}/(Ilim)))$ **(1.16)**

where, nact is the dynamic activation voltage I_{fc} is the operating current of the system in A, nc the number of cells, V_{fc} the voltage of a single cell in V/cell, $P_{hydrogen\_anode}$ and $P_{oxygen\_cathode}$ stands for the hydrogen and oxygen pressure in bar or atm, $C_{oxygen\_interface}$ is the concertation of the interface in mol/m^3, ne number of electrons, Far Faraday's constant and $Ilim$ maximum allowable current

Furthermore, the thermal equations of the PEM fuel cell system are important and given as.

❖ Chemical Thermal Energy

$Q_{chem_{fc}} = ((DH_{WATER\_o} - 0.5 * DH_{OXYGEN\_o} - DH_{HYDROGEN\_o}) + (Cp_{fc_{WATER}} - 0.5 * Cp_{fc_{OXYGEN}} - Cp_{fc_{HYDROGEN}}) * (T_{out\_fc} - T_{ref})) * Rfc$ **(1.17)**

❖ Electrical Thermal Energy

$Q_{elec_{fc}} = nc * I_{fc} * (1.253 - Vfc)$ **(1.18)**

❖ Radiation

$Q_{rad_{fc}} = e * sig * Afc * nc * ((T_{out\_fc}{}^4) - T_{amb}{}^4)$ **(1.19)**

❖ Coolant Thermal Energy

$Q_{cool_{fc}} = (Ufc * Afc * nc) * (T_{out\_fc} - T_{cool\_fc})$ **(1.20)**

The presented equations collectively form the **thermal energy balance of a PEM fuel cell system**, aiming to quantify all major sources of heat generation and dissipation during operation. The concept is based on capturing how energy enters, transforms, and exits the system through chemical, electrical, radiative, and convective mechanisms.

- The **chemical thermal energy** equation calculates the heat released from the exothermic electrochemical reaction that forms water, incorporating both the reaction enthalpy and temperature-dependent sensible heat contributions.
- The **electrical thermal energy** term quantifies heat losses due to internal inefficiencies in the fuel cell. It reflects the portion of electrical potential lost as heat when the actual operating voltage is lower than the theoretical maximum.
- The **radiative heat loss** accounts for thermal energy dissipated to the environment via infrared radiation, following the Stefan–Boltzmann law, which is critical at higher temperatures.
- Lastly, the **coolant thermal energy exchange** describes the system's ability to remove excess heat through forced convection, thus stabilizing the fuel cell temperature during prolonged operation.

Together, these expressions provide a framework for modeling the thermal dynamics of the system, which is essential for efficiency optimization, control strategy development, and ensuring safe and stable fuel cell performance.

After presenting the main equations that will accompany the main dynamic model, the **non-linear differential equations** for temperature and species concentration is provided in detail.

The operating temperature T_{out} of the fuel cell during operation is given as:

$$\frac{dT_{out}}{dt} = \frac{(-Q_{chem_{fc}} + Q_{elec_{fc}} - Q_{cool_{fc}} - Q_{rad_{fc}})}{m_{fc} * Cp_{fc}} \quad \textbf{(1.21)}$$

The outlet concentrations at the anode and cathode of the hydrogen, oxygen, nitrogen, and water components are given by the following four equations (H_2, O_2, N_2, H_2O):

$$\frac{dC_{out,H_2}}{dt} = \frac{Q_{in\_anode} * C_{in\_fc\_hydrogen} - Q_{out\_anode} * C_{out\_fc\_hydrogen\_an} - Rfc}{V\_anode} \quad \textbf{(1.22)}$$

$$\frac{dC_{out,O_2}}{dt} = \frac{Q_{in\_cathode} * C_{in\_fc\_oxygen\_cat} - Q_{out\_cathode\_gas} * C_{out\_fc\_oxygen\_cat} - 0.5Rfc}{V\_cathode} \quad \textbf{(1.23)}$$

$$\frac{dC_{out,N_2}}{dt} = \frac{Q_{in\_cathode} * C_{in\_fc\_nitrogen\_cat} - Q_{out\_cathode\_gas} * C_{out\_fc\_nitrogen\_cat}}{V\_cathode} \quad \textbf{(1.24)}$$

$$\frac{dC_{out,H_2O}}{dt} = \frac{(Q_{in\_cathode} * C_{in\_fc\_water\_cat} - Q_{out\_cathode\_liquid} * C_{out\_fc\_water\_cat} + Rfc}{V\_cathode} \quad \textbf{(1.25)}$$

The fuel cell will require to be cooled during operation. Hence, the coolant temperature $Tcool$ is given by the following equation:

$$\frac{dT_{cool}}{dt} = \frac{m_{cool\_fc} * cp_{cool\_fc} * (T_{cool\_in\_fc} - T_{cool\_fc}) + Q_{cool\_fc}}{p_{cool\_fc} * V_{cool\_fc} * cp_{cool\_fc}} \quad \textbf{(1.26)}$$

The dynamic activation voltage of the fuel cell is preferred to be studied in relation to the static activation voltage, as it provides the dynamic operating form of the fuel cell, and its equation is given as:

$$\frac{dn_{act}}{dt} = (I_{fc}/Capacity) * (1 + n_{act}/V_{act}) \quad \textbf{(1.27)}$$

The results of the simulation in the programming environment of the MATLAB will be given for comparison with those of the linear model as well as the space-state model. In the next section will be analyzed the Taylor linearization method and its application to the creation of the linear model [16].

1.2 Linearization of the PEM fuel cell model

The operation of the fuel cell is described by a dynamic mathematical model composed of non-linear differential equations. These equations involve derivatives of state variables and non-linear terms, making them difficult to solve using classical analytical methods. To address this challenge, the linearization method using Taylor series expansion around equilibrium points is applied.

The general form of the Taylor series for a variable x around an equilibrium point $\bar{x}$, where $f(\bar{x}) = 0$, is given by:

$$f(x) = f(\bar{x}) + \frac{df}{dx}(x - \bar{x}) + \frac{1}{2}\frac{d^2f}{dx^2}(x - \bar{x})^2 + \ldots \quad \textbf{(1.28)}$$

In cases where $x \approx \bar{x}$, higher-order terms can be neglected, so the equation is approximated as:

$$f(x) \approx f(\bar{x}) + a \cdot (x - \bar{x}) \quad \textbf{(1.29)}$$

Since $f(\bar{x}) = 0$, the above form simplifies to:

$$\dot{x} = a \cdot (x - \bar{x}) \quad \textbf{(1.30)}$$

Defining the disturbance variable $\delta x = x - \bar{x}$, the linearized model is described as:

$$\dot{x} = a \cdot \delta x \quad \textbf{(1.31)}$$

This linearization is locally valid and only applies near the equilibrium point. Its accuracy depends on how non-linear the original function is.

In the case of the fuel cell model, the system's behavior is described by nineteen state variables and corresponding non-linear equations. Specifically, these equations model the output temperature of the fuel cell (T_{out}), the operating current (I_{fc}), output voltage, and the concentrations of hydrogen (H_2), oxygen (O_2), nitrogen (N_2), and water (H_2O) at the anode and cathode outputs.

To handle such a multi-variable system, linearization is extended to multiple state variables x_j and inputs u_j, through the use of partial derivatives, given by the expression:

$$f_i(x_1, \ldots, x_n, u_1, \ldots, u_n) \approx \sum \left(\frac{\partial f_i}{\partial x_j}\right)(x_j - \bar{x}_j) + \sum \left(\frac{\partial f_i}{\partial u_j}\right)(u_j - \bar{u}_j) \quad \textbf{(1.32)}$$

Here, the equation f_i describes the behavior of the i-th state variable, and the equilibrium points $\bar{x}_j$, $\bar{u}_j$ are values that make all system equations equal to zero. Each equation of the dynamic model will be linearized according to this expression, in order to enable modeling through programming code in the MATLAB environment. In the next chapter will present the solution and the comparison of the linear model with the non-linear one [8] [16].

1.3 State-space model description

In this section the basic description of the linearized dynamic model through state-space representation is provided. The state equations are a description in the time field and which can be exploited for a wide variety of systems.

The system of equations of state describing a space model - state model will be of the form:

$$\dot{\boldsymbol{x}} = \boldsymbol{A} \cdot \boldsymbol{x}(\boldsymbol{t}) + \boldsymbol{B} \cdot \boldsymbol{u}(\boldsymbol{t})$$

$$\boldsymbol{y} = \boldsymbol{C} \cdot \boldsymbol{x}(\boldsymbol{t}) + \boldsymbol{D} \cdot \boldsymbol{u}(\boldsymbol{t})$$

A, B, C and D are called matrices of the state space. In the system of equations, the matrix A is defined as square matrix of the system (state matrix) with dimensions $n \times n$ which represents the physical system. Matrix B is of dimension $n \times m$ and is called the input matrix. In the output equations y, matrix C is called the outputs and is $k \times n$ dimensional, and finally the matrix D is called the output matrix and is $k \times n$ dimensional (In this system D matrix equals to 0) [16] [17].

In fuel cell modeling, nineteen state variables are used to represent the system that results in a 19 × 19 state matrix A. The system inputs at the beginning consist of seven variables like input molar flow rates (F_{in}), coolant flow rate (m_{cool}), the overall temperature (T_{in_fc}) and the reference temperature (T_{ref}). The input concentrations are considered to be indirect ones because they only depend on the molar flow rates and their adjustment. Hence, the concentrations do not belong to the active input set used in the formulation of the state-space model since they do not contribute or have a negligible effect towards the dynamic response.

Table 1.1: Input variables

INPUT VARIABLES		
u_1	$F_{in\_fc\_hydrogen}$	Hydrogen molar flow rate, will be used in control
u_2	$F_{in\_fc\_oxygen\_cat}$	Oxygen molar flow rate
u_3	$F_{in\_fc\_nitrogen\_cat}$	Nitrogen molar flow rate
u_4	$F_{in\_fc\_water\_cat}$	Water molar flow rate, equals to zero
u_5	T_{in_fc}	Overall inlet temperature
u_6	T_{ref}	Reference temperature, used as dummy input
u_7	m_{cool}	Coolant flow rate, will be used in control

Table 1.2: Output variables

OUTPUT VARIABLES		
y1	T_{out}	Operating temperature
y2	C_{out,H_2}	Hydrogen outlet concentration
y3	C_{out,O_2}	Oxygen outlet concentration
y4	C_{out,N_2}	Nitrogen outlet concentration
y5	C_{out,H_2O}	Water outlet concentration
y6	T_{cool}	Coolant temperature
y7	$nact$	Dynamic activation voltage
y8	I_{fc}	Operating current
y9	P_{fc}	Operating power
y10	F_{out,H_2}	Hydrogen outlet flow rate
y11	F_{out,O_2}	Oxygen outlet flow rate
y12	F_{out,N_2}	Nitrogen outlet flow rate
y13	F_{out,H_2O}	Water outlet flow rate

There are also 6 auxiliary variables not stated at the above table. Thus, the input matrix B is defined with a size 19 × 3, which corresponds to the two molar flow inputs (Hydrogen and Oxygen) and the coolant flow. The system output y(t) is defined according to the operator's requirement to measure certain state variables. Output

matrix C is constructed in terms of ones and zeros such that ones indicate the state variables to be measured and zeros for the non-interest variables.

Similarly, feedthrough matrix D is also defined in terms of ones and zeros for inputs, depending upon whether they affect the output directly.

Also, certain elements of the A and B matrices are represented by complex expressions that are coefficients in the differential equations of the model. To avoid making matrix representation too complicated, these are shortened by dummy variables a-s, ba-bl and 1-7, the letter represents the row of A and B matrices respectively and the numbers the column. This is merely for convenience in the presentation of the model without any loss of accuracy.

Below are given in detail the tables that will represent the space model for the PEM type hydrogen cell as follows:

Table 1.3: Matrix A physical system dimensions 19*19

$$A = \begin{bmatrix} a1 & 0 & 0 & 0 & 0 & a6 & 0 & a8 & 0 & 0 & 0 & 0 & 0 & 0 & 0 & 0 & 0 & 0 & 0 \\ b1 & b2 & 0 & 0 & 0 & 0 & 0 & b8 & 0 & b10 & 0 & 0 & 0 & 0 & 0 & 0 & 0 & 0 & 0 \\ c1 & 0 & c3 & 0 & 0 & 0 & 0 & 0 & 0 & 0 & c11 & c12 & 0 & 0 & 0 & 0 & 0 & 0 & 0 \\ d1 & 0 & 0 & d4 & 0 & 0 & 0 & 0 & 0 & 0 & d11 & d12 & 0 & 0 & 0 & 0 & 0 & 0 & 0 \\ 0 & 0 & 0 & 0 & e5 & 0 & 0 & e8 & 0 & 0 & 0 & 0 & e13 & 0 & 0 & 0 & 0 & 0 & 0 \\ f1 & 0 & 0 & 0 & 0 & f6 & 0 & 0 & 0 & 0 & 0 & 0 & 0 & 0 & 0 & 0 & 0 & 0 & 0 \\ 0 & 0 & 0 & 0 & 0 & 0 & 0 & 0 & 0 & 0 & 0 & 0 & 0 & 0 & 0 & 0 & 0 & 0 & 0 \\ 0 & 0 & 0 & 0 & 0 & 0 & 0 & g8 & 0 & 0 & 0 & 0 & 0 & 0 & 0 & 0 & 0 & 0 & 0 \\ 0 & 0 & 0 & 0 & 0 & 0 & 0 & h8 & h9 & 0 & 0 & 0 & 0 & 0 & 0 & 0 & 0 & 0 & 0 \\ 0 & 0 & 0 & 0 & 0 & 0 & 0 & i8 & 0 & i10 & 0 & 0 & 0 & 0 & 0 & 0 & 0 & 0 & 0 \\ 0 & 0 & 0 & 0 & 0 & 0 & 0 & j8 & 0 & 0 & j11 & 0 & 0 & 0 & 0 & 0 & 0 & 0 & 0 \\ 0 & 0 & 0 & 0 & 0 & 0 & 0 & 0 & 0 & 0 & 0 & k12 & 0 & 0 & 0 & 0 & 0 & 0 & 0 \\ 0 & 0 & 0 & 0 & 0 & 0 & 0 & l8 & 0 & 0 & 0 & 0 & l13 & 0 & 0 & 0 & 0 & 0 & 0 \\ 0 & 0 & 0 & 0 & 0 & 0 & 0 & 0 & 0 & 0 & 0 & 0 & 0 & 0 & 0 & 0 & 0 & 0 & 0 \\ 0 & 0 & 0 & 0 & 0 & 0 & 0 & 0 & 0 & 0 & 0 & 0 & 0 & 0 & 0 & 0 & 0 & 0 & 0 \\ 0 & 0 & 0 & 0 & 0 & 0 & 0 & 0 & 0 & 0 & 0 & 0 & 0 & 0 & 0 & 0 & 0 & 0 & 0 \\ 0 & 0 & 0 & 0 & 0 & 0 & 0 & 0 & 0 & 0 & 0 & 0 & 0 & 0 & 0 & 0 & 0 & 0 & 0 \\ 0 & 0 & 0 & 0 & 0 & 0 & 0 & 0 & 0 & 0 & 0 & 0 & 0 & 0 & 0 & 0 & 0 & 0 & 0 \\ 0 & 0 & 0 & 0 & 0 & 0 & 0 & s8 & 0 & 0 & 0 & 0 & 0 & 0 & 0 & 0 & 0 & 0 & s19 \end{bmatrix}$$

Table 1.4: Matrix input B dimensions 19*7

$$B = \begin{bmatrix} 0 & 0 & 0 \\ bb1 & 0 & 0 \\ bc1 & 0 & 0 \\ bd1 & 0 & 0 \\ 0 & 0 & 0 \\ 0 & bf2 & bf3 \\ 0 & 0 & 0 \\ bh1 & 0 & 0 \\ 0 & 0 & 0 \\ bj1 & 0 & 0 \\ bk1 & 0 & 0 \\ bl1 & 0 & 0 \\ 0 & 0 & 0 \\ 0 & 0 & 0 \\ 0 & 0 & 0 \\ 0 & 0 & 0 \\ 0 & 0 & 0 \\ 0 & 0 & 0 \\ 0 & 0 & 0 \end{bmatrix}$$

Table 1.5: Matrix output C dimensions 19*19

$$C = \begin{bmatrix} 1 & 0 & 0 & 0 & 0 & 0 & 0 & 0 & 0 & 0 & 0 & 0 & 0 & 0 & 0 & 0 & 0 & 0 & 0 \\ 0 & 1 & 0 & 0 & 0 & 0 & 0 & 0 & 0 & 0 & 0 & 0 & 0 & 0 & 0 & 0 & 0 & 0 & 0 \\ 0 & 0 & 1 & 0 & 0 & 0 & 0 & 0 & 0 & 0 & 0 & 0 & 0 & 0 & 0 & 0 & 0 & 0 & 0 \\ 0 & 0 & 0 & 1 & 0 & 0 & 0 & 0 & 0 & 0 & 0 & 0 & 0 & 0 & 0 & 0 & 0 & 0 & 0 \\ 0 & 0 & 0 & 0 & 1 & 0 & 0 & 0 & 0 & 0 & 0 & 0 & 0 & 0 & 0 & 0 & 0 & 0 & 0 \\ 0 & 0 & 0 & 0 & 0 & 1 & 0 & 0 & 0 & 0 & 0 & 0 & 0 & 0 & 0 & 0 & 0 & 0 & 0 \\ 0 & 0 & 0 & 0 & 0 & 0 & 1 & 0 & 0 & 0 & 0 & 0 & 0 & 0 & 0 & 0 & 0 & 0 & 0 \\ 0 & 0 & 0 & 0 & 0 & 0 & 0 & 1 & 0 & 0 & 0 & 0 & 0 & 0 & 0 & 0 & 0 & 0 & 0 \\ 0 & 0 & 0 & 0 & 0 & 0 & 0 & 0 & 1 & 0 & 0 & 0 & 0 & 0 & 0 & 0 & 0 & 0 & 0 \\ 0 & 0 & 0 & 0 & 0 & 0 & 0 & 0 & 0 & 1 & 0 & 0 & 0 & 0 & 0 & 0 & 0 & 0 & 0 \\ 0 & 0 & 0 & 0 & 0 & 0 & 0 & 0 & 0 & 0 & 1 & 0 & 0 & 0 & 0 & 0 & 0 & 0 & 0 \\ 0 & 0 & 0 & 0 & 0 & 0 & 0 & 0 & 0 & 0 & 0 & 1 & 0 & 0 & 0 & 0 & 0 & 0 & 0 \\ 0 & 0 & 0 & 0 & 0 & 0 & 0 & 0 & 0 & 0 & 0 & 0 & 1 & 0 & 0 & 0 & 0 & 0 & 0 \\ 0 & 0 & 0 & 0 & 0 & 0 & 0 & 0 & 0 & 0 & 0 & 0 & 0 & 1 & 0 & 0 & 0 & 0 & 0 \\ 0 & 0 & 0 & 0 & 0 & 0 & 0 & 0 & 0 & 0 & 0 & 0 & 0 & 0 & 1 & 0 & 0 & 0 & 0 \\ 0 & 0 & 0 & 0 & 0 & 0 & 0 & 0 & 0 & 0 & 0 & 0 & 0 & 0 & 0 & 1 & 0 & 0 & 0 \\ 0 & 0 & 0 & 0 & 0 & 0 & 0 & 0 & 0 & 0 & 0 & 0 & 0 & 0 & 0 & 0 & 1 & 0 & 0 \\ 0 & 0 & 0 & 0 & 0 & 0 & 0 & 0 & 0 & 0 & 0 & 0 & 0 & 0 & 0 & 0 & 0 & 1 & 0 \\ 0 & 0 & 0 & 0 & 0 & 0 & 0 & 0 & 0 & 0 & 0 & 0 & 0 & 0 & 0 & 0 & 0 & 0 & 1 \end{bmatrix}$$

The variables denoted as a-s in matrices A and B, which represent mathematical expressions, are further analyzed in **Appendix**, located at the end of the main body of the study. In many state-space models, in addition to the four core matrices A, B, C, and D, a fifth matrix is often included to represent disturbances that may affect the system. This matrix is known as the disturbance matrix E. However, in this particular linear

mode, no type of disturbance is considered for any of the state variables. As a result, this matrix is deemed negligible and is considered to be zero.

The developed state-space model is implemented in the MATLAB programming environment for the purpose of simulation. Through this implementation, graphical representations of the state variable responses are generated and will later be compared with those of the linear model in Chapter 2. This follows a similar methodology previously applied when comparing the dynamic and linearized models [8] [16].

1.4 Transfer functions (Gp) in State Space model

The term **"transfer function"**, often denoted as **Gp(s)** in the Laplace domain, refers to a mathematical model that describes the dynamic behavior of a system or process in relation to its inputs and outputs.

A SISO continuous-time transfer function is expressed as the ratio:

$$G_p(s) = \frac{N(s)}{D(s)},$$

of polynomials $N(s)$ and $D(s)$, called the numerator and denominator polynomials, respectively. [22]

In the previous section, the state-space model was analyzed in detail. From this model, the transfer functions Gp will be derived for each of the main variables of the system. These transfer functions will represent the dynamic relationship between the system's inputs and its key state variables, enabling further analysis and controller design based on the behavior of each individual component.

- Starting from the transfer function of the temperature (T_{out}):

$$Gp_{T_{out}} = \frac{\left(0.3826 - 1.2307 * 10^{-4}\right) * (2515 * s + 8556) - 0.1429}{60.2599 * s^2 + 205.4189 * s + 1} \quad \textbf{(1.33)}$$

- The transfer function of the Coolant Temperature (T_{cool}):

$$Gp_{T_{cool}} = \frac{964.2418}{(5 * s + 1) * (60.2599 * s\text{^}2 + 205.4189 * s + 1)} - \frac{4.7322 * 10^{-6}}{(60.2599 * s^2 + 205.4189 * s + 1)} - \frac{3.3226 * (145.0910 * s + 1)}{(60.2599 * s^2 + 205.4189 * s + 1)} \quad \textbf{(1.34)}$$

- Transfer functions of the operating current and the delivered power are:

$$Gp_{I_{fc}} = \frac{1.0149 * 10^9}{(5 * s + 1)} \quad \textbf{(1.35)}$$

$$Gp_{P_{fc}} = \frac{1.5767 * 10^5}{(5 * s + 1)^2} \quad \textbf{(1.36)}$$

- Transfer functions of the line-molecular flow rates of the components at the anode and cathode outlet are:

$$Gp_{F_{outH_2}} = \frac{1}{(4 * s + 1)} - \frac{0.9340}{(4 * s + 1) * (5 * s + 1)} \quad \textbf{(1.37)}$$

$$Gp_{F_{outO_2}} - \frac{0.4670}{(4*s+1)*(5*s+1)} + \frac{1}{(4*s+1)} \qquad \textbf{(1.38)}$$

Below is a schematic representation of the relationship between the input variables u and the output variables y, indicating how each input affects specific outputs. This mapping highlights the direct influence paths within the system, providing insight into the input–output coupling structure.

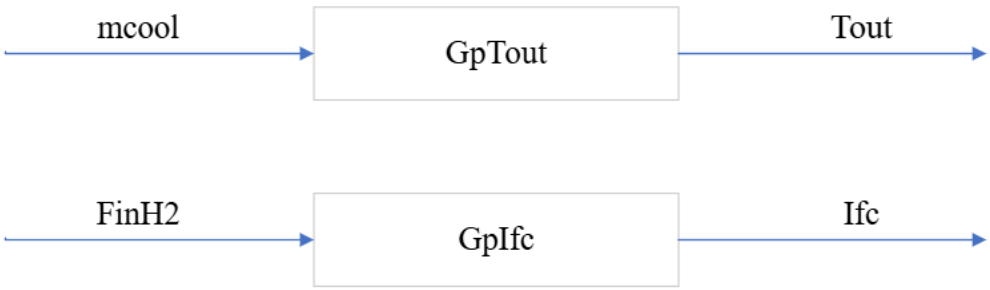

Picture 1.1: Schematic Representation of Input–Output Variable Relationships

Chapter 2: SIMULATION OF PEM FUEL CELL SYSTEM MODELS

Chapter introduction

In this chapter, the simulation results for each of the models previously analyzed will be presented Additionally, a further simulation will be carried out by changing two key system variables — the hydrogen inlet molar flow rate (Fin_H_2) and the coolant flow rate (m_{cool}) — by ±30%. In this way, we will achieve two goals a) check their suitability as control variables and b) ensure that the linear model is a descent representation of the original linear model [14] [16].

2.1 Comparison of Models

All three models that have been developed share the same initial parameters and data, which are presented in detail in the table below:

Table 2.1: Initial parameters for all models

Description	Symbol	Value and Units
Volume of anode	V_anode	$50*10^{-3}$ m^3
Volume of cathode	V_cathode	$50*10^{-3}$ m^3
Number of cells	nc	28
Number of electrons	ne	2
Faraday constant	Far	96485 Cb/mol
Fuel cell efficiency	n_f	1.0
Fuel cell pressure	P_fc	1.3 bar
Inlet temperature of fuel cell	Tfc_in	298 K
Universal gas constant	Rg	8.314 J/K·mol
Gas constant in	Rg_1	$82.06 \cdot 10^{-6}$ atm·L/mol·K
Formation enthalpy of water	DH_WATER_o	$-241.82 \cdot 10^3$ J/mol
Formation enthalpy of oxygen	DH_OXYGEN_o	0 J/mol

Formation enthalpy of hydrogen	DH_HYDROGEN_o	0 J/mol
Reference temperature	Tref	298 K
Heat transfer coefficient of fuel cell	Ufc	900 J/m²·s·K
Fuel cell surface area	Afc	$5 \cdot 10^{-3}$ m²
Coolant density	pcool_fc	1.25 kg/m³
Volume of coolant	Vcool_fc	0.01 m³
Specific heat capacity of coolant	cpcool_fc	1006 J/K·kg
Emissivity	e	0.9
Stefan-Boltzmann constant	sig	$5.678 \cdot 10^{-8}$ J/s·K⁴·m²
Ambient temperature	Tamb	293 K
Capacity	Capacity	1000 F
Maximum current	Ilim	100 A
Oxygen-hydrogen ratio	O_H	1.5
Inlet coolant temperature	Tcool_in_fc	298 K
Time constant	t_fc	5 s
Specific heat capacity of anode	Cp_anode	2247.2 J/K·kg
Specific heat capacity of cathode	Cp_cathode	1032 J/K·kg
Utilization factor	Ut_factor	0.934
Fuel cell mass	m_fc	0.16×nc + 2.1
Fuel cell heat capacity	Cp_fc	100×nc J/K·kg
Internal resistance	Rohm	2.2e-3 Ohm
Parameters describing the electrochemical actions of the anode/cathode		
Model constant	x1	-0.944
Model constant	x2	0.00354
Model constant	x3	-1.91e-4
Model constant	x4	7.6e-5
Model constant	x5	3.3e-3
Model constant	x6	-1.2e-5
Model constant	x7	1.1e-6

Starting the simulation with the non-linear model, the initial data must be taken into account conditions of the state variables at time t=0. These data are presented in the following table:

Table 2.2: Initial parameters of the non-linear model

State Variables	Initial conditions (t=0)
Tout_fc	298 K
Cout_fc_hydrogen	10^{-9} mol/m^3
Cout_fc_oxygen_cat	10^{-9} mol/m^3
Cout_fc_nitrogen_cat	0.0 mol/m^3
Cout_fc_water_cat	0.0 mol/m^3
Tcool_fc	298 K
nact	0.0 V
Ifc	0.0 A
Pfc	0.0 W
Fout_fc_hydrogen	0.0 mol/s
Fout_fc_oxygen_cat	0.0 mol/s
Fout_fc_nitrogen_cat	0.0 mol/s
Fout_fc_water_cat	0.0 mol/s
V_fc_real	0.0 V
Fout_fc_hydrogen_an_help	0.0 mol/s
Fout_fc_oxygen_cat_help	0.0 mol/s
Fout_fc_nitrogen_cat_help	0.0 mol/s
Fout_fc_water_cat_help	0.0 mol/s
Tsp	298 K

The graphic plots to be studied will not concern all nineteen state variables that describe the fuel cell model, but rather those considered to be the most critical for the analysis of the model. These include the temperature T_{out}, the heat removal by the cooling medium in terms of T_{cool} temperature the line-molecular flow rates of hydrogen F_{out_H2} and oxygen F_{out_O2}, as well as the operating current I_{fc} and the generated power P_{fc}. Since, the efforts of this study is the development of the control system, the analysis of the following figures is not provided in detail.

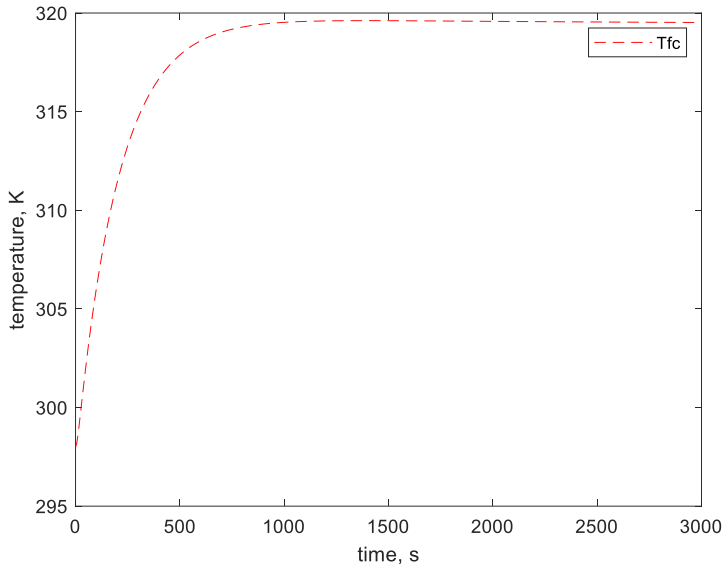

Figure 2.1: Operating temperature curve diagram of T_{out} PEMFC.

The T_{out} curve appears to have a smooth and rapid path towards stabilization at approximately 319.5 K.

The temperature T_{cool} exhibits fluctuations as it does not stabilize at a single value but oscillates between 303.8 K and 304.7 K (non-linearity).

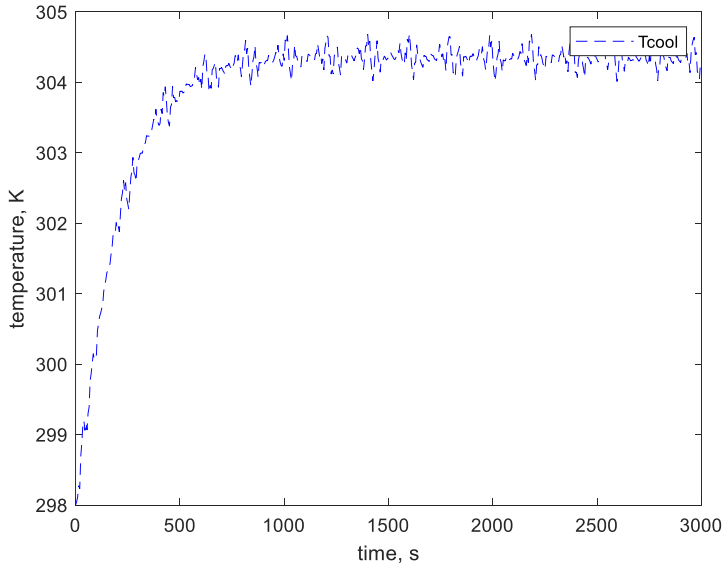

Figure 2.2: Cooling temperature curve diagram of T_{out} PEMFC.

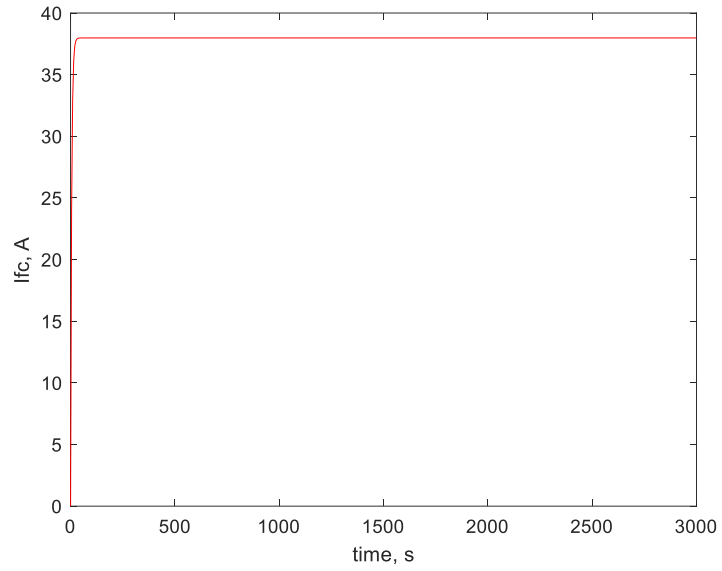

Figure 2.3: Operating current curve diagram of I_{fc} PEMFC.

The curve that describes the operating current Ifc based on the values of the parameters that have been defined is given in the form above. The response of the operating current, according to the dynamic model, shows rapid stabilization at a value 37.9 A.

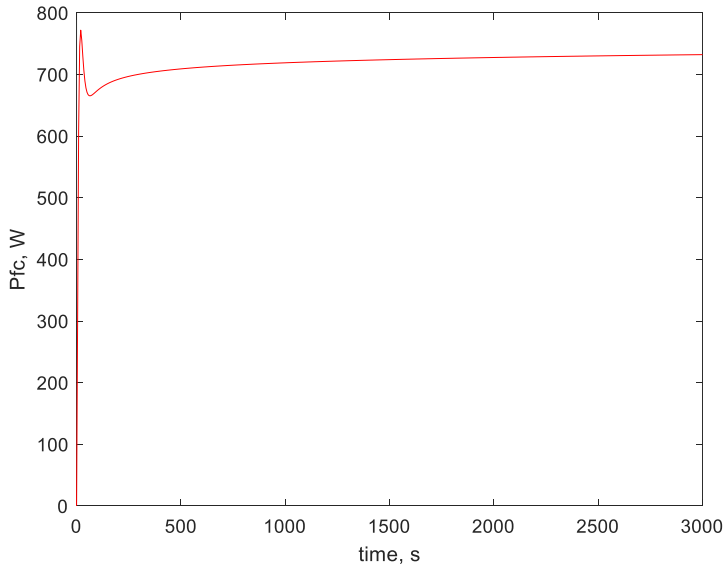

Figure 2.4: Power output curve diagram of P_{fc} PEMFC.

In contrast to the graph of Ifc, there is initially a low overshoot that reaches the levels of 800W before its stabilization at 732.2W.

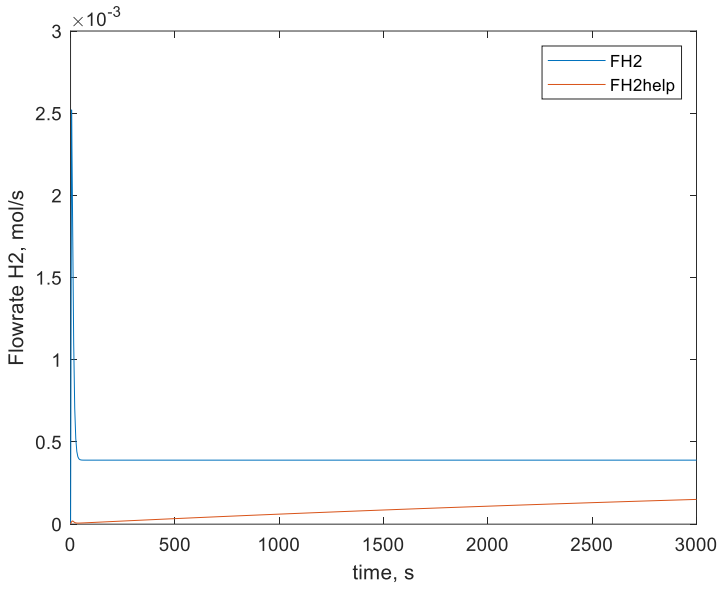

Figure 2.5 Molar flow curve diagram of H_2 at the outlet of PEMFC.

The hydrogen flow at the outlet of the fuel cell is directly related to the fuel inlet flow as well as the operating current. The outlet flow stabilizes at 0.000389 mol/s relatively quickly and remains constant for the rest of the simulation.

The oxygen flow at the outlet of the cell shows a negligible overshoot at the start of simulation, but it almost immediately stabilizes its value at 0.0061 mol/s and remains unchanged.

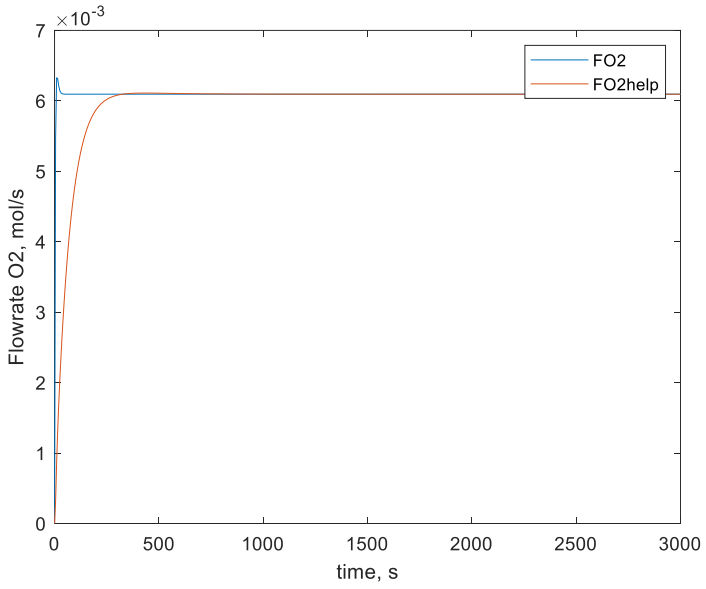

Figure 2.6 Molar flow curve diagram of O_2 at the outlet of PEMFC.

2.3 Solution and Presentation of Diagrams of the Linear Model

Starting the section on the solution of the linear model, it is deemed necessary to define the steady-state points for each state variable, as well as the new form these variables will now take. More specifically, since there are nineteen state variables, there will be fourteen equilibrium points (as the remaining five are auxiliary in the code and will not concern us), the values of which are given in the table below:

Table 2.3: Steady-State Variables and Their Values

State variable	Steady-state variable	Value
Tout_fc	Tout_fc_ss	319.52 K
Cout_fc_hydrogen_an	Cout_fc_hydrogen_an_ss	18.919 mol/m^3
Cout_fc_oxygen_cat	Cout_fc_oxygen_cat_ss	7.572 mol/m^3
Cout_fc_nitrogen_cat	Cout_fc_nitrogen_cat_ss	41.364 mol/m^3
Cout_fc_water_cat	Cout_fc_water_cat_ss	329.106 mol/m^3
Tcool_fc	Tcool_fc_ss	304.278 K
Ifc	Ifcss	37.978 A
Pfc	Pfcss	732.196 W
Fin_fc_hydrogen	Fin_fc_hydrogen_ss	0.0059 mol/s
Fout_fc_hydrogen_an	Fout_fc_hydrogen_an_ss	0.00039 mol/s
Fout_fc_oxygen_cat	Fout_fc_oxygen_cat_ss	0.00609 mol/s
Fout_fc_nitrogen_cat	Fout_fc_nitrogen_cat_ss	0.03329 mol/s
Fout_fc_water_cat	Fout_fc_water_cat_ss	0.00551 mol/s
Tsp	Tspss	0.53*Ifcss + 26.01 + 273 K

Following the definition of the steady-state variables, the simulation of the linear model is carried out, accompanied by a graphical representation of its results, similarly to the procedure applied to the nonlinear model. Subsequently, a comparative analysis of the two models is performed in order to validate their dynamic similarity.

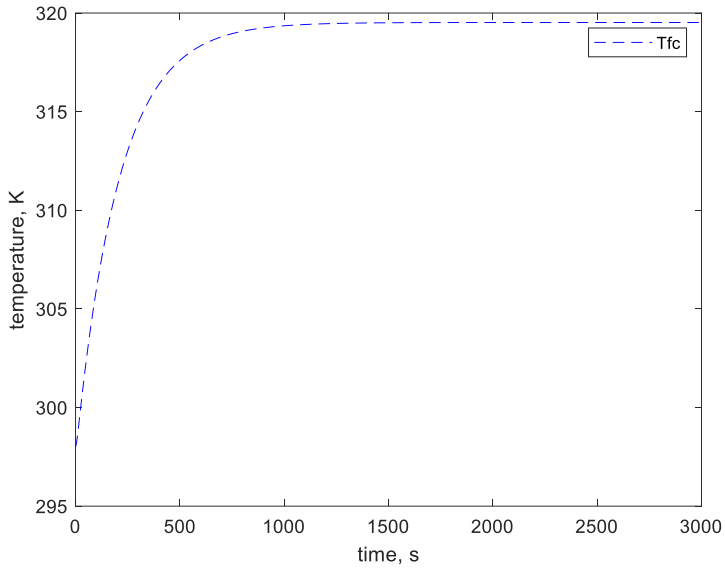

Figure 2.7: Operating temperature curve diagram of T_{out} PEMFC for Linear Model.

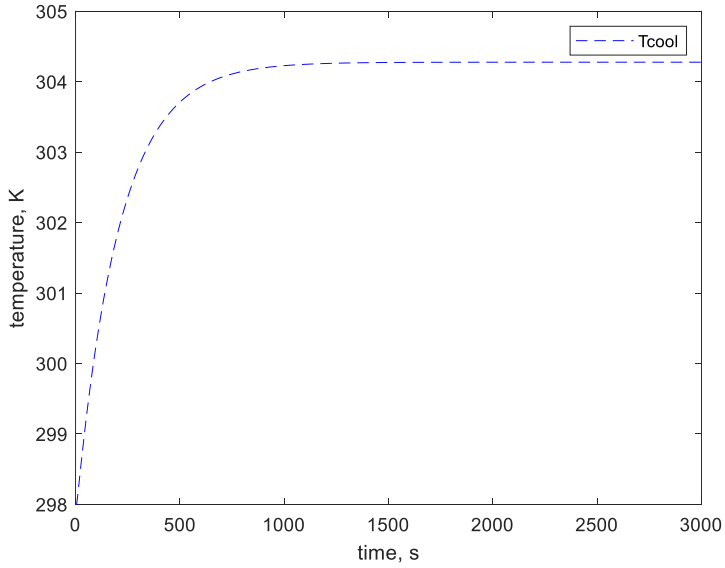

Figure 2.8: Cooling temperature curve diagram of T_{cool} PEMFC for Linear Model.

The operating temperature curve in the linear model perfectly coincides with that of the nonlinear model in Fig. 2.1. The curve gradually increases and subsequently stabilizes at exactly the same values and with the same response characteristics as observed in the dynamic system diagram. The simulation exhibited no deviations or delayed response, a fact which demonstrates the reliability of the linear model in accurately capturing the state variable that describes the operating temperature of the fuel cell.

Similar to the operating temperature curve, the cooling temperature also demonstrates accuracy compared to the nonlinear model in Fig. 2.2. However, the significant

difference compared to the dynamic model is that it does not exhibit the same fluctuations and instead stabilizes at a value slightly above 304 K, specifically at 304.27 K. This gives the impression that the linear model operates with greater accuracy regarding the cooling temperature.

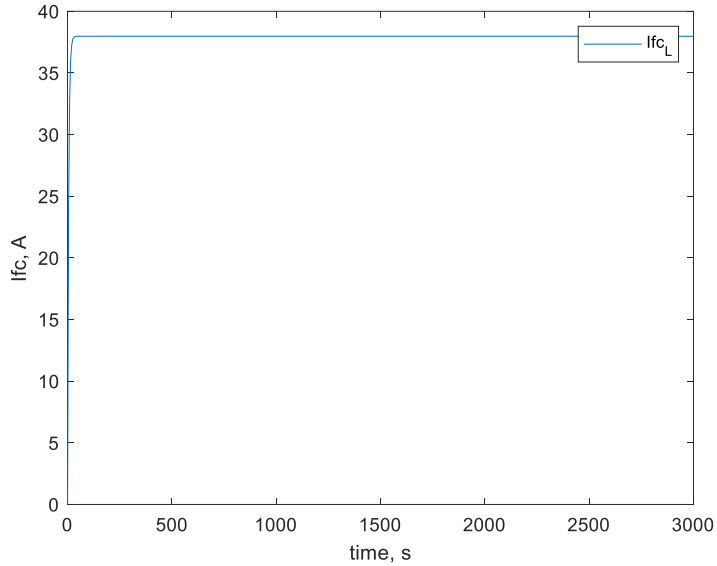

Figure 2.9: Operating current curve diagram of I_{fc} PEMFC for Linear Model.

The curve describing the current behavior according to the linear model appears identical to that of the nonlinear system in Fig. 2.3. Its response is equally fast, reaching approximately 40 A with absolute accuracy compared to the dynamic model. The operating current eventually stabilizes at 37.9 A by the end of the simulation.

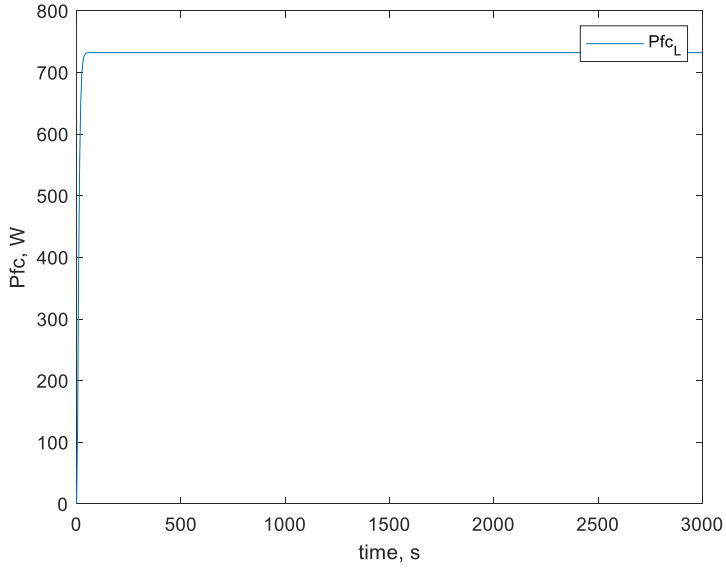

Figure 2.10: Power output curve diagram of P_{fc} PEMFC for Linear Model.

Similarly, the behavior of the power variable exhibits exceptional accuracy and a very fast response in reaching the value at which it stabilizes, namely 732.1 W. It differs significantly from the corresponding graph of the nonlinear model in terms of the initial overshoot, which is not present in the case of the linear model. However, the model stabilizes the power at the same level as the previous one.

The diagram of the molar flow rate of H_2 at the outlet also appears identical to the corresponding one in the nonlinear model in Fig. 2.5. The instantaneous increase observed at the beginning of the simulation, which appears as a peak, as well as the subsequent stabilization of the variable's value, are presented in the same manner as in the corresponding diagram of the dynamic model. Similarly, the diagram of the molar flow rate of O_2 at the outlet is exactly the same, showing no difference whatsoever from the previous model.

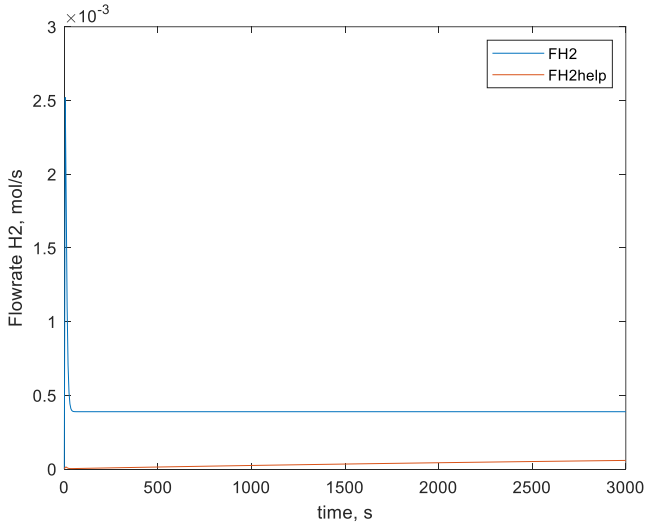

Figure 2.11 Molar flow curve diagram of H_2 at the outlet of PEMFC Linear Model.

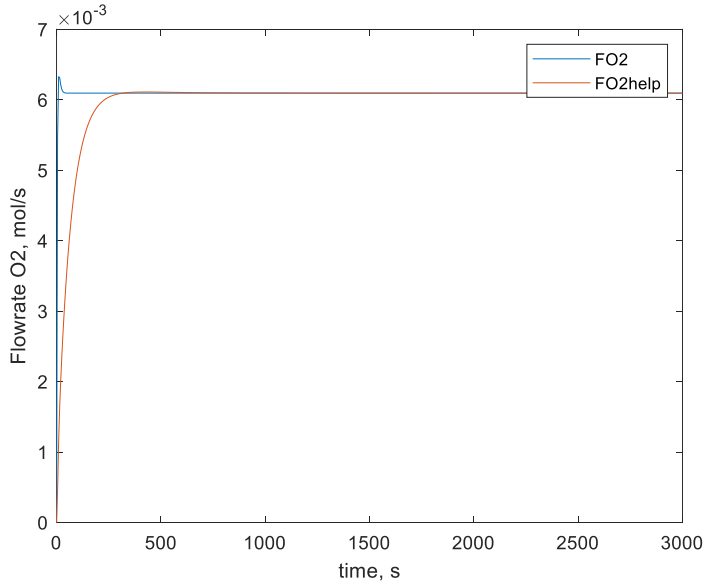

Figure 2.12 Molar flow curve diagram of O_2 at the outlet of PEMFC Linear Model.

In summary, the comparison of the response curve diagrams between the nonlinear and the linear model leads to the conclusion that the accuracy and reliability of the linear model in simulating the overall operation of the fuel cell—through the state variables that describe it—are indisputable. This conclusion is drawn from the analysis conducted above regarding the most critical variables, as well as from the rest of the graphical representations produced during the simulation. The linear model has the capability to capture the dynamic behavior of the fuel cell without missing almost any detail in the response curves of each variable, and thus it successfully reflects its realistic performance.

2.4 Solution and Presentation of Diagrams of the Space-State Model

In this section, the graphical representations of the state-space model are presented and are expected to be identical to the previous ones. The results shown below will be compared with those of the linear model and, by extension, with the dynamic model's plots in terms of the similarity of their curves. In order for the graphs produced by the state-space model to be considered accurate, they must demonstrate similar response and shape to those of the linear model. This determination will be based on the visual comparison of the corresponding graphical representations.

In the previous chapter, the matrices defining the state-space model were presented in detail, so will proceed with its solution.

As with the previous models, in the state-space model as well, the final operating temperature starts from the initially defined point and smoothly reaches the stabilization point slightly below 320 K. An exact similarity with the previous models is also observed. Regarding the graph for the system's cooling temperature, it appears to be identical to the graph in Figure 2.8 but with a significant difference compared to Figure 2.2. Just like in the linear model, in the state-space one as well, the graph smoothly approaches the stabilization point at 304.28 K without any fluctuation or deviation.

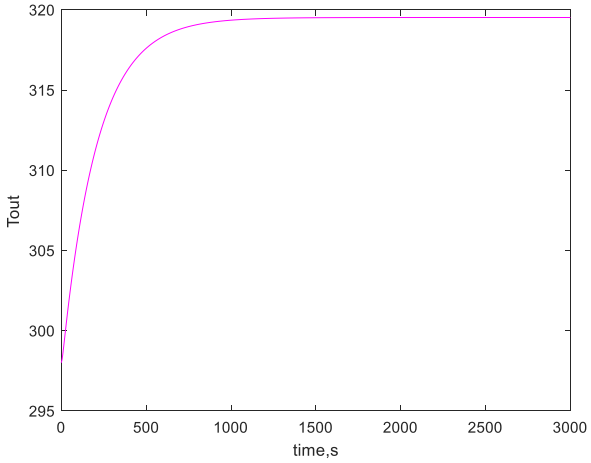

Figure 2.13: Operating temperature curve diagram of T_{out} PEMFC for State-Space Model.

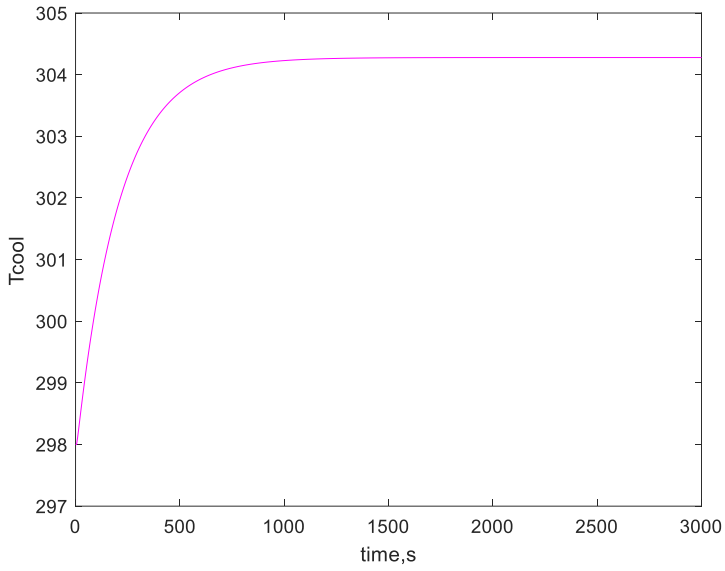

Figure 2.14: Cooling temperature curve diagram of T_{cool} PEMFC for State-Space Model.

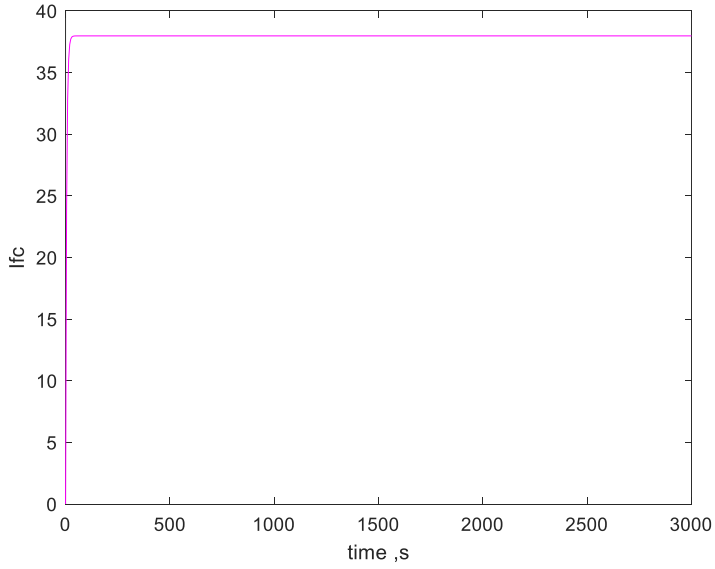

Figure 2.15: Operating current curve diagram of I_{fc} PEMFC for Stae-Space Model.

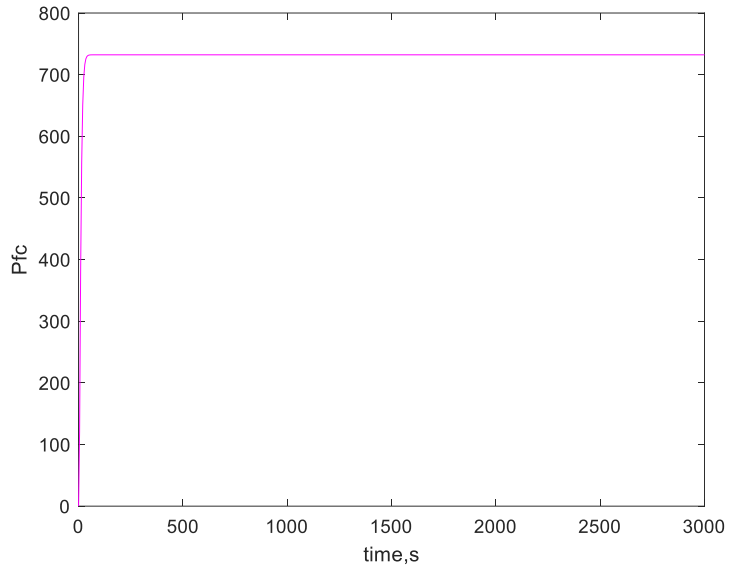

Figure 2.16: Power output curve diagram of P_{fc} PEMFC for State-Space Model.

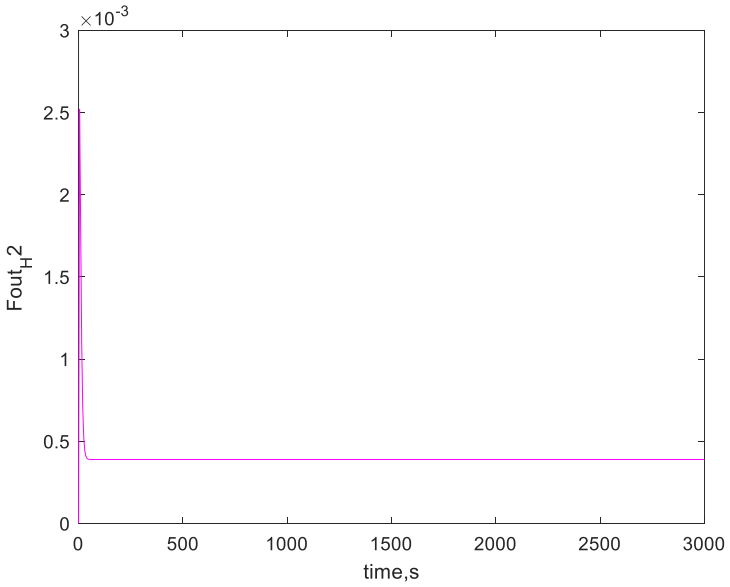

Figure 2.17 Molar flow curve diagram of H_2 at the outlet of PEMFC State-Space Model.

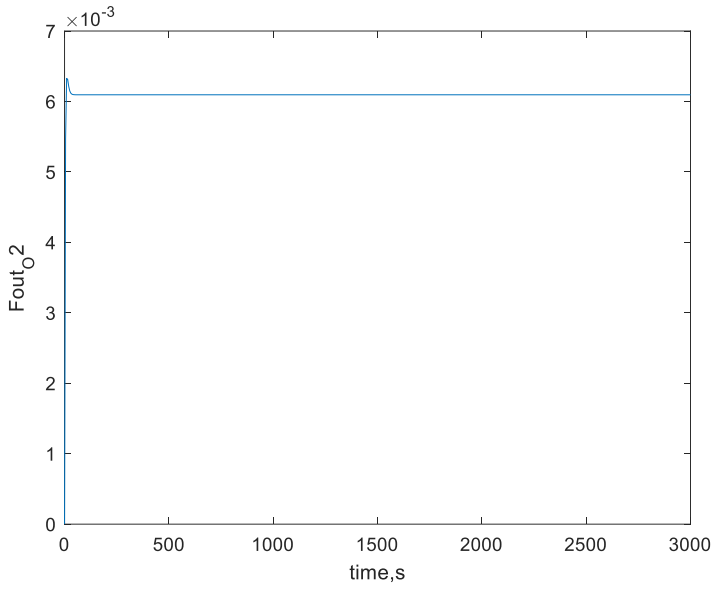

Figure 2.18 Molar flow curve diagram of O_2 at the outlet of PEMFC State-Space Model.

2.5 Simulation of Tests on the PEM Fuel Cell System

The goal of this section is to further test and verify the accuracy of the three mathematical models developed throughout this study, as well as to assess their consistency in representing the behavior of the variables that define the operation of the fuel cell under investigation. More specifically, the tests conducted on the dynamic, linear, and state-space models will involve variations in specific parameters that directly affect the fuel cell's variables and indirectly its overall performance. The parameters considered in these tests are the molar flow rate of hydrogen at the inlet Fin_H_2 and the flow rate of the cooling medium m_{cool} [16].

2.5.1 Increase of Hydrogen Inlet Molar Flow Rate Fin_H_2 by +30%

The first test applied across all three models involves a 30% increase in the hydrogen inlet flow rate. This test aims to evaluate the impact of this change on the three most critical state variables that characterize the fuel cell system's behavior. Each model—dynamic, linear, and state-space—will be analyzed for consistency and accuracy in reflecting these variable responses under the modified input condition.

The following is an analysis of the graphs, beginning with the operating temperature variable T_{out} for each of the three models, as shown below:

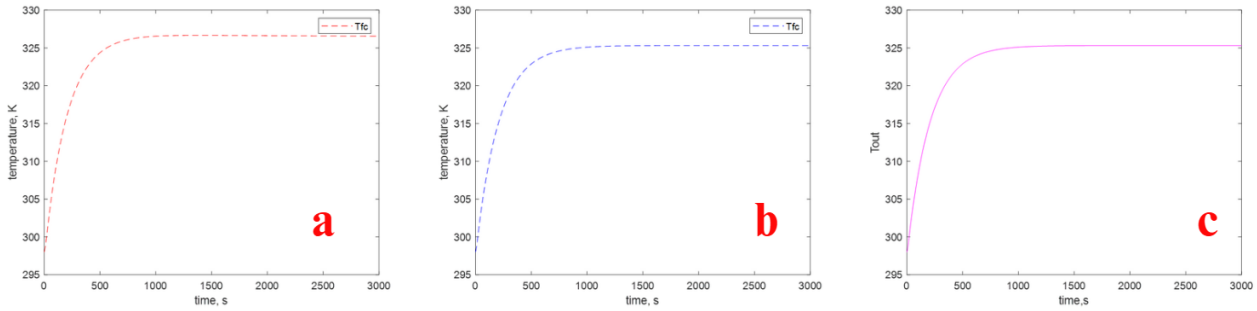

Figure 2.19 Operating temperature curves T_{out} from the non-linear model (curve a), linear model (curve b), and state-space model (curve c).

Starting with the operating temperature, it is easily observed that all three models are in complete agreement both in terms of response and the shape of the curve. Beginning at 298 K, the temperature rises smoothly and stabilizes for the remainder of the simulation just above 325 K. Continuing with the heat removed by the cooling medium (Tcool), the corresponding graphs are presented below.

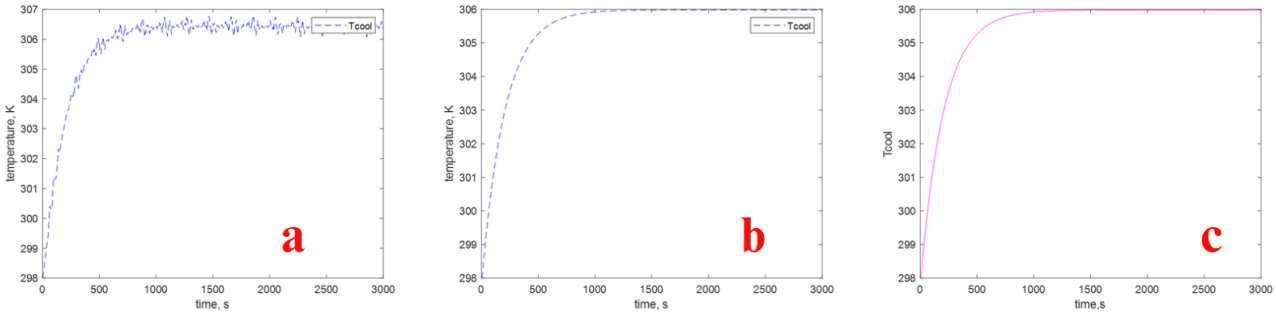

Figure 2.20 Cooling temperature curves T_{cool} from the non-linear model (curve a), linear model (curve b), and state-space model (curve c).

As observed, the non-linear model does not stabilize at a fixed value but rather oscillates around approximately 306 K. In contrast, the other two models exhibit identical behavior, as they both initiate from the same starting point and converge smoothly to a steady-state value slightly above 306 K.

Below is the analysis of the operating current curves that produced by the three models are given below as follows.

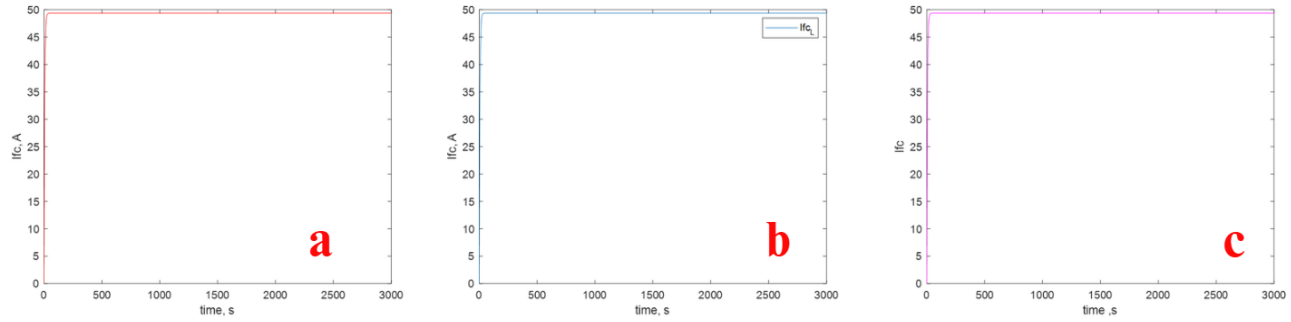

Figure 2.21 Operating current curves I_{fc} from the non-linear model (curve a), linear model (curve b), and state-space model (curve c).

The graphs of all three models follow the same trajectory and are identical. They all reach the steady-state point almost instantaneously, slightly below 50 A, and remain at that point until the end of the simulation.

At the end of this specific simulation, the graphs for the power output are presented below.

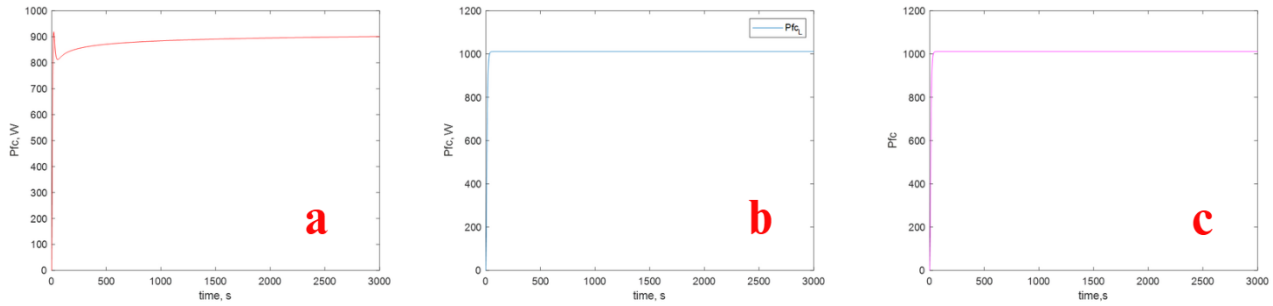

Figure 2.21 Power output curves P_{fc} from the non-linear model (curve a), linear model (curve b), and state-space model (curve c).

The power output curves produced by the three models in response to this variation exhibit overall similarity. They all increase rapidly, reaching approximately 900 W with comparable response characteristics. However, a slight dip is observed in the nonlinear model around 800 W, followed by a gradual return to values close to 900 W. A further noteworthy difference is that, in the state-space model, the generated power exceeds this level and eventually stabilizes at approximately 1000 W, indicating a higher final steady-state output compared to the other models.

Table 2.4: Steady-State Points for the increase of Fin_H2 +30%

Steady-State Points (Increase Fin_H2 +30%)			
Variables	**Non-Linear**	**Linear**	**State-Space**
Tout	326.55 K	326.15 K	325.18 K
Tcool	306.06 – 306.76 K	306.23 K	305.98 K
Ifc	49.37 A	49.37 A	49.37 A
Pfc	900.7143 W	1011.27 W	1011.27 W

Here we have to highlight that this deviation between the non-linear and the linear (and state-space) model is due to the fact that the voltage is calculated based on the equations provided in chapter 1, where a mean value was used in the other models (was not included in the lineartization).

2.5.2 Decrease of Hydrogen Inlet Molar Flow Rate Fin_H_2 by -30%

In this part, a reduced fuel flow rate by 30% (i.e., the input variable for H_2 supply, Fin_H_2) is applied to the fuel cell, essentially the inverse scenario of the first part of the section. A similar analysis of the resulting diagrams from the models will follow, along with a comparison of their mutual agreement. The state variables under examination are presented in the same order as in the previous section, beginning with the operating temperature T_{out}.

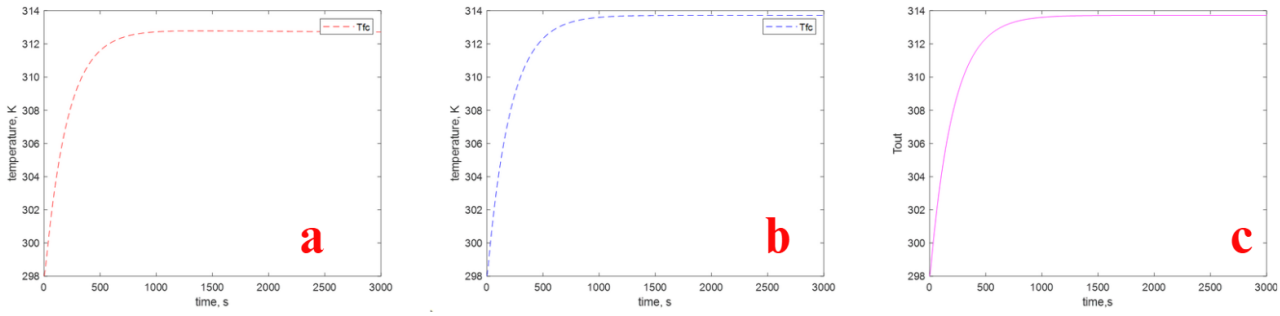

Figure 2.22 Operating temperature curves T_{out} from the non-linear model (curve a), linear model (curve b), and state-space model (curve c).

It is observed from the above curves that the first two models are identical to each other, both in shape and in the steady-state value, which stabilizes slightly above 312 K. In contrast, the state-space model exhibits a similar response pattern; however, its steady-state value differs significantly, reaching just below 314 K. The analysis for the cooling temperature will then be presented.

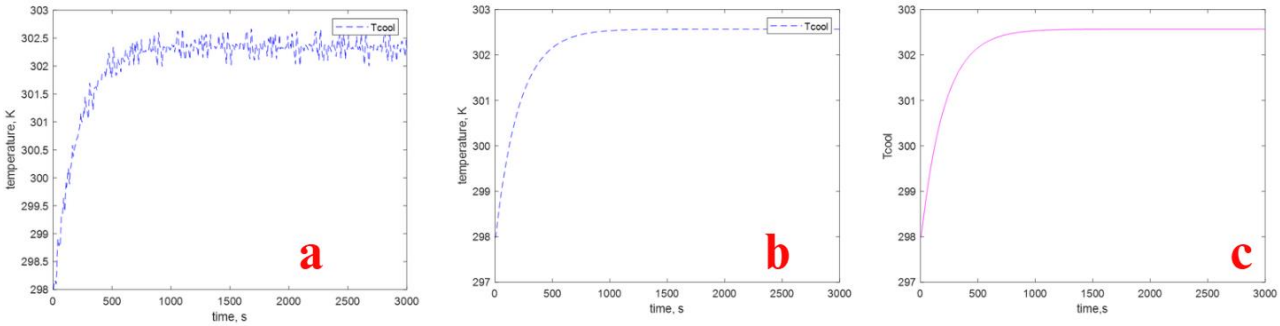

Figure 2.23 Cooling temperature curves T_{cool} from the non-linear model (curve a), linear model (curve b), and state-space model (curve c).

As observed in the previous case, a significant deviation is noted in the nonlinear model, which fails to stabilize at a specific value and instead oscillates within the range of 302 to 302.5 K. In contrast, the other two models exhibit identical behavior, showing no discernible differences and maintaining a stable response.

Below is the analysis of the operating current and operating power curves generated by the three models. The corresponding plots are presented as follows.

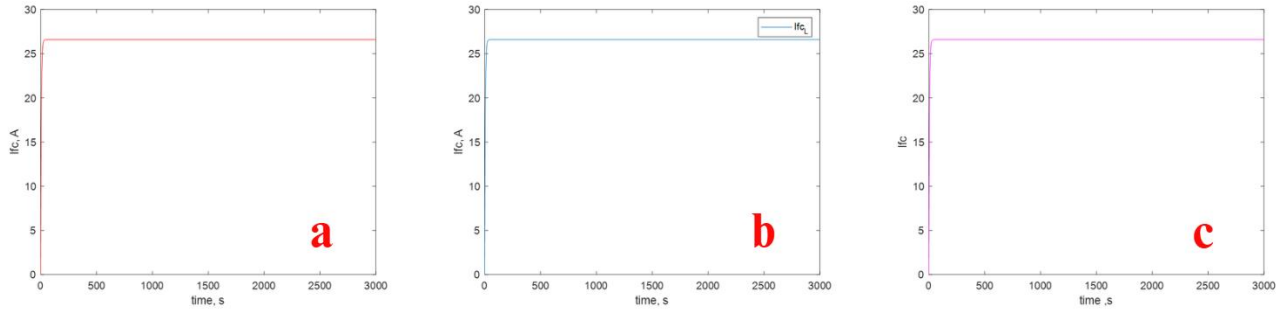

Figure 2.24 Operating current curves I_{fc} from the non-linear model (curve a), linear model (curve b), and state-space model (curve c).

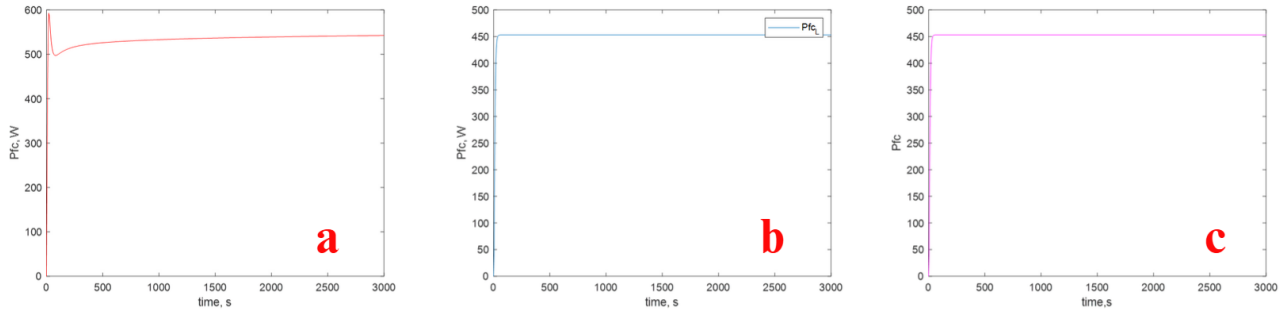

Figure 2.25 Power output curves P_{fc} from the non-linear model (curve a), linear model (curve b), and state-space model (curve c).

As demonstrated above, the curves of the operating current are identical across all three models, showing no differences whatsoever. However, in the case of the operating power curves, a distinction once again emerges in the non-linear model. Specifically, it exhibits an abrupt rise followed by a slight but sharp drop before beginning to stabilize.

Table 2.5: Steady-State Points for the decrease of Fin_H2 -30%

Steady-State Points (Decrease Fin_H2 -30%)			
Variables	**Non-Linear**	**Linear**	**State-Space**
Tout	312.72 K	313.15 K	313.73 K
Tcool	302.00 – 302.65 K	302.40 K	302.57 K
Ifc	26.58 A	26.58 A	26.58 A
Pfc	542.56 W	453.12 W	453.12 W

2.5.3 Increase of the coolant flow m_{cool} by +30%

In this section and the next, coolant flow changes in the system. Initially the flow will be increased by 30%, which means that the system will be able to dissipate greater amounts of heat, making it cooler and cooler and reduce the overall operating temperature. At the same time, this change is not expected to affect the electrical load and power and power produced by the cell (or only as an insignificant effect), as shown in the graphs below. It is highlighted that this temperature refers to the overall stack temperature (unified across the stack).

Initially, the operating temperature of the T_{out} system and the cooling temperature T_{cool} will be presented.

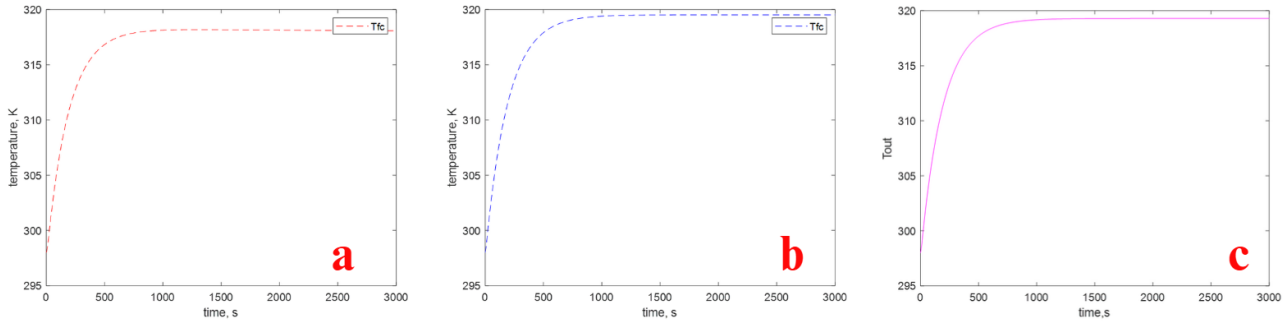

Figure 2.26 Operating temperature curves T_{out} from the non-linear model (curve a), linear model (curve b), and state-space model (curve c).

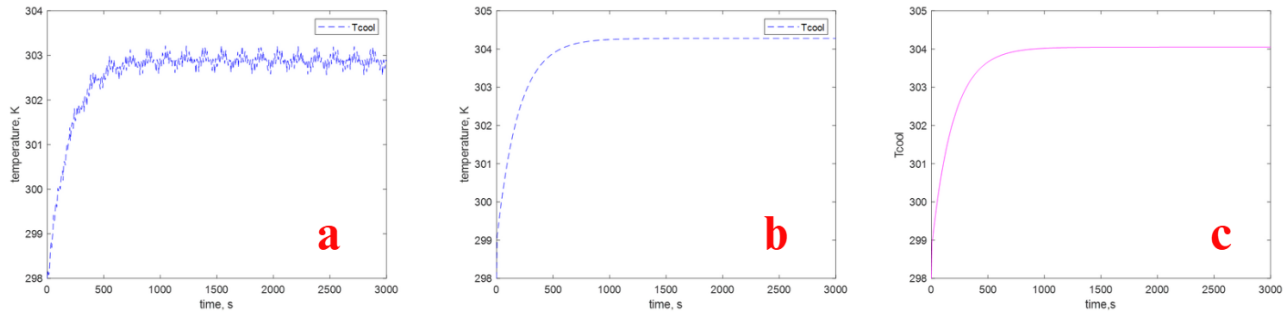

Figure 2.27 Cooling temperature curves T_{cool} from the non-linear model (curve a), linear model (curve b), and state-space model (curve c).

As can be clearly identified, the output temperature curves of the system are nearly identical across all of the three models. The only noticeable difference lies in the non-linear model, where the simulation stabilizes at a slightly lower temperature compared to the others. However, this deviation is minor and does not significantly affect the reliability or validity of the system's performance. Regarding the system's cooling temperature, slightly more variations are observed among the models; however, these differences remain small and insufficient to compromise the system's overall reliability. Specifically, the expected fluctuations appear again in the non-linear model, as noted in previous simulations. Aside from this, with closer examination, one can discern a further distinction: the linear model reaches and stabilizes at its steady-state point more rapidly, and this point is marginally higher compared to that of the state-space model.

The following section presents the curves for the system's output operating current and power.

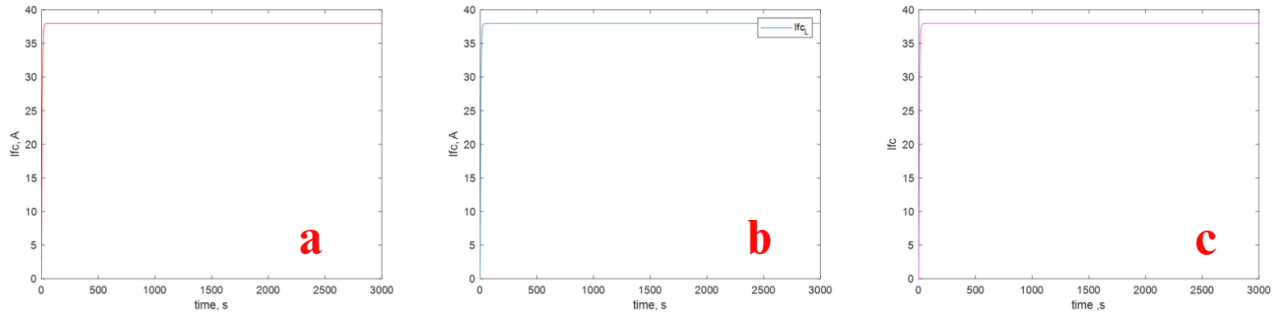

Figure 2.28 Operating current curves I_{fc} from the non-linear model (curve a), linear model (curve b), and state-space model (curve c).

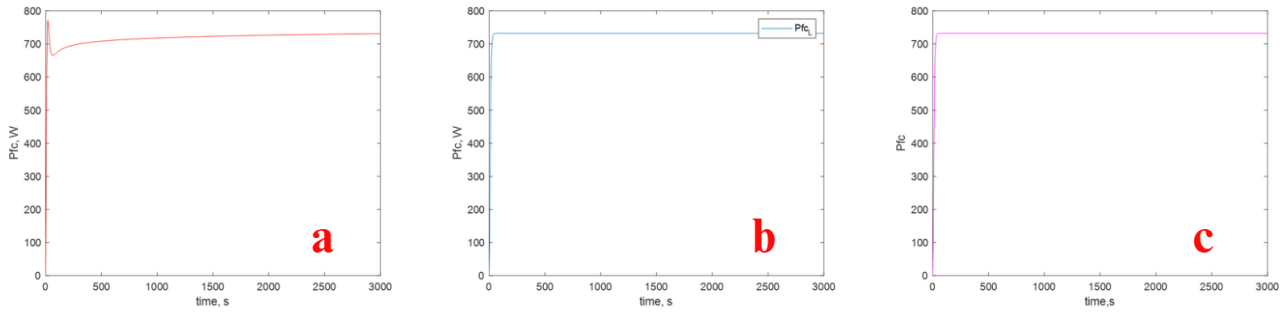

Figure 2.29 Power output curves P_{fc} from the non-linear model (curve a), linear model (curve b), and state-space model (curve c).

The behavior of the operating current variable remains consistent across all three models, mirroring its response in the initial scenario without any parameter changes. The curves exhibit no variation in shape or response time and yield comparable results among the models. Similarly, with regard to the operating power of the system, no significant deviations are identified across the models—except for the nonlinear model, which exhibits a typical initial irregularity at the beginning of the simulation. However, it ultimately converges to the same steady-state value as the other two models.

Table 2.6: Steady-State Points for the increase of m_{cool} +30%

Steady-State Points (Increase m_{cool} +30%)			
Variables	**Non-Linear**	**Linear**	**State-Space**
Tout	318.08 K	319.52 K	319.14 K
Tcool	302.55 – 303.21 K	304.28 K	304.05 K
Ifc	37.98 A	37.98 A	37.98 A
Pfc	731.21 W	732.20 W	732.20 W

2.5.4 Decrease of the coolant flow m_{cool} by -30%

In the fourth and final variation applied to the system, which involves a 30% reduction in the coolant flow rate, the variables of each model will be compared, as previously, in terms of their behavior and graphical representation. The variables expected to be

directly affected are the operating temperature (T_{out}) and the heat removed by the coolant (T_{cool}), both of which are theoretically anticipated to exhibit a relative increase.

Starting with the analysis of the operating temperature across the three models, the corresponding plots are presented as follows:

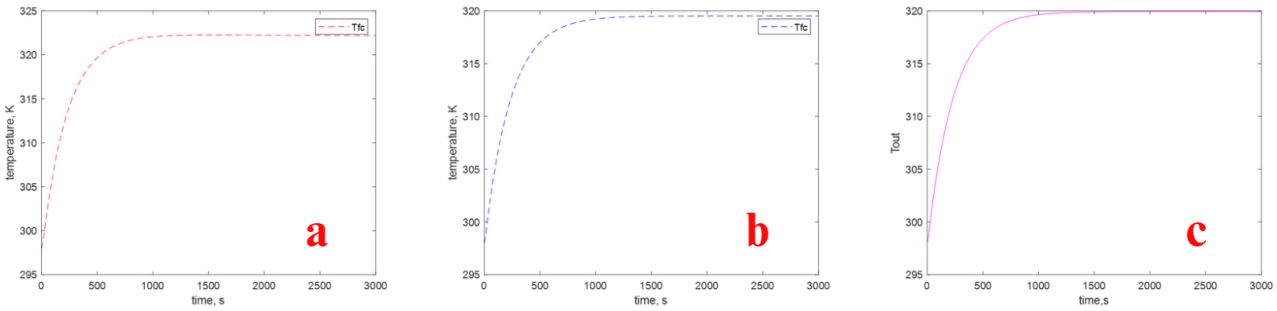

Figure 2.30 Operating temperature curves T_{out} from the non-linear model (curve a), linear model (curve b), and state-space model (curve c).

As it is shown, all three models exhibit similar behavior in both form and response time. The only notable difference lies in the final stabilization point of the nonlinear model, which levels off at a slightly higher value—approximately 322 K—compared to the other two models, which stabilize just below 320 K. However, this deviation is considered negligible and does not compromise the overall reliability of the system. The analysis of the cooling temperature follows next.

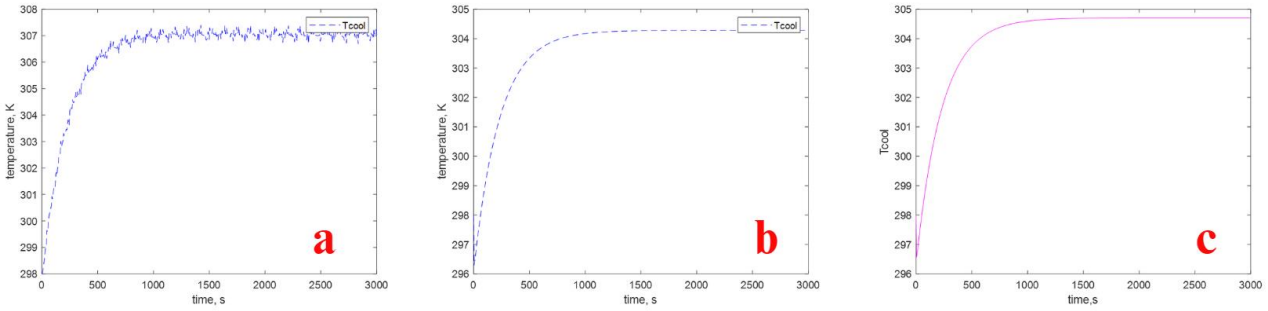

Figure 2.31 Cooling temperature curves T_{cool} from the non-linear model (curve a), linear model (curve b), and state-space model (curve c).

Exactly as observed in previous cases, the curves for the coolant temperature show no deviation between the linear model and the state-space model. The same fluctuation is observed in the nonlinear model, oscillating around 307 K, consistent with earlier simulations. Moreover, another noticeable difference is the steady-state value: the nonlinear model reaches at a slightly higher temperature of approximately 307 K, compared to around 304.6 K in the other two models.

The final variables to be analyzed are the operating current and the power of the system.

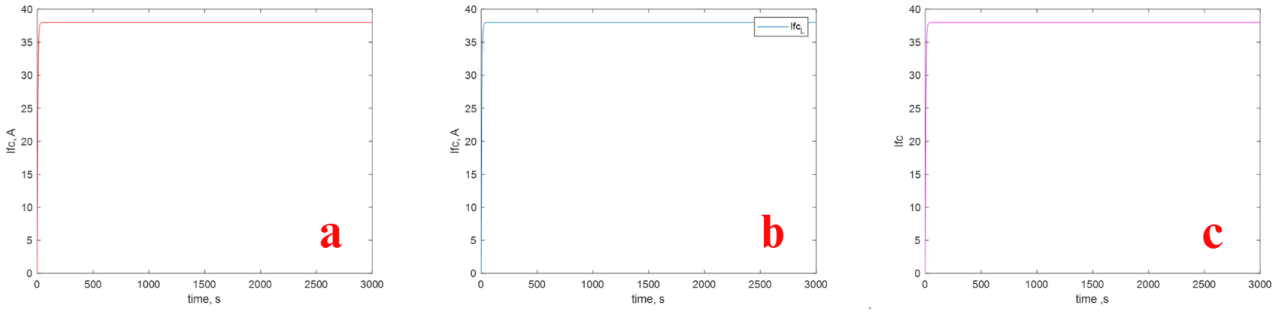

Figure 2.32 Operating current curves I_{fc} from the non-linear model (curve a), linear model (curve b), and state-space model (curve c).

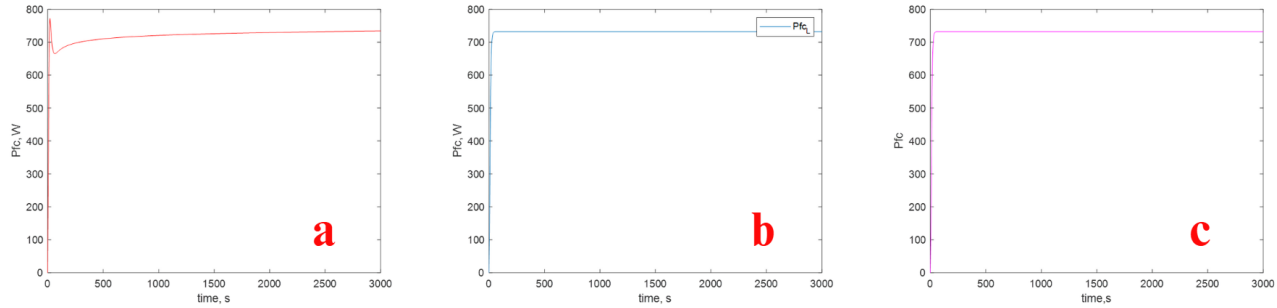

Figure 2.33 Power output curves P_{fc} from the non-linear model (curve a), linear model (curve b), and state-space model (curve c).

The operating current variable is not affected by the variation introduced in this section. Consequently, the shape of the three curves produced by the models remains identical to that of the previous scenario. These results are considered entirely satisfactory.

Similarly, the operating power variable also remains unaffected by this change. Each model produces a curve consistent in shape with those presented in the previous section, where the power increases and stabilizes slightly above 700 W. The only noticeable difference is a slight irregularity at the beginning of the simulation in the nonlinear model. However, this behavior is consistent with previous cases and does not affect the overall reliability of the system.

Table 2.7: Steady-State Points for the decrease of m_{cool} -30%

Steady-State Points (Decrease m_{cool} -30%)			
Variables	**Non-Linear**	**Linear**	**State-Space**
Tout	322.18 K	319.52 K	319.94 K
Tcool	306.69 – 307.40 K	304.28 K	304.70 K
Ifc	37.98 A	37.98 A	37.98 A
Pfc	734.03 W	732.20 W	732.20 W

Chapter 3: ANALYSIS ON THE CONTROL SYSTEM OF THE PEM FUEL CELL

Chapter introduction

In this chapter, an extensive analysis will be carried out, with the aim of introducing a suitable controller for the as-modelled fuel cell. More specifically, a theoretical framework of control systems will be presented, followed by an analysis of the most well-known controllers, which will be classified based on their effectiveness and suitability.

Subsequently, the control process for the existing system will be described — that is, which variables will be subject to control and how the modeling was performed within the MATLAB environment. Finally, the results derived from MATLAB simulations will be presented as a comparison between the different controllers. The most efficient(s) will be selected.

3.1 Theory on Control Systems

Control systems theory is a fundamental discipline in engineering and applied sciences that focuses on the behavior of dynamical systems and the design of controllers to regulate system outputs. It provides a mathematical framework and practical tools to ensure that systems perform desired tasks with stability, accuracy, and robustness despite internal uncertainties and external disturbances. Control theory finds applications across diverse fields, including mechanical, chemical, process and electrical engineering, biological networks, and industrial automation. At its core, a control system consists of several key components:

- the plant, which is the physical system or process to be controlled, such as a motor, chemical reactor, or biological organ; In our case it is the fuel cell.
- the sensor, which measures the output or state of the plant; In our case the sensors will measure the temperature and the power/current.
- the controller, which adjusts the control input based on the difference between the desired reference and the measured output (error);
- the actuator, which implements the control input to influence the plant; In our case is the coolant flow and the hydrogen flow

The primary objective of control theory is to design the controller so that the system output follows a desired reference signal while maintaining stability and performance criteria.

Control systems are broadly categorized into open-loop and closed-loop (feedback) systems. *Feedback control* uses output measurements to dynamically adjust inputs, providing robustness against disturbances and model uncertainties. This feedback loop is central to modern control theory and enables self-correcting behavior. *Feedforward*

control anticipates disturbances and compensates without relying on output measurements, often complementing feedback control to improve overall system performance. Mathematical modeling is fundamental in control theory, where system dynamics are described by differential equations or other types of models. Two primary frameworks are commonly used: the transfer function approach, which represents systems in the frequency domain using Laplace transformations to facilitate analysis of stability, frequency response, and transient behavior; and the state-space representation, which describes systems using a set of first-order differential equations in vector form, enabling analysis of multi-input multi-output (MIMO) systems and modern control design techniques [23].

Proportional (P), Proportional-Integral (PI), and Proportional-Integral-Derivative (PID) controllers are fundamental types of feedback controllers widely used in control systems. The P controller indduces an output proportional to the current error, providing a simple and fast response but often leaving a steady-state error (offset). The PI controller adds an integral term to eliminate this offset by integrating the error over time, improving steady-state accuracy, but potentially slowing the response. The PID controller further incorporates a derivative term that predicts future error trends, enhancing stability and transient response by reducing overshoot and oscillations [24].

The Ziegler–Nichols method involves a strategy where increasing the proportional gain leads the system output to oscillates continuously at the ultimate gain Ku with period Pu. Controller parameters are then adjusted using empirical formulas derived from Ku and Pu. This method typically results in aggressive tuning with faster response but can cause significant overshoot and oscillations.

The Tyreus-Luyben method modifies the Ziegler–Nichols approach to yield more conservative tuning parameters, aiming for less oscillatory and more robust control. It uses the same Ku and Pu values but applies different formulas to calculate the PI and PID gains, generally resulting in smoother responses with reduced sensitivity to process changes.

In practice, the choice between these tuning methods depends on the specific system requirements: Ziegler–Nichols is often preferred when faster response is critical and some overshoot is acceptable, while Tyreus-Luyben is favored for processes requiring smoother control and greater stability [11] [17].

3.2 Modelling of the Control System

In this section, the control modeling procedure will be presented, along with the methodology through which the system identified the appropriate controllers. More specifically, two distinct control loops will be implemented for the current system. The first concerns the regulation of the hydrogen inflow in relation to the generated current, while the second focuses on the coolant flow rate as it affects the operating temperature. Each control objective will be addressed through dynamic analysis and tuning strategies aimed at achieving stability, responsiveness, and effective disturbance rejection.

3.2.1 Root Locus Analysis for Power Control

One of the fundamental challenges in the design of automatic control systems lies on determining the appropriate parameters of a controller, so that the closed-loop system poles are placed at desired locations in the complex plane. These pole locations directly govern the system's stability and significantly influence its transient response characteristics.

In its simplest form, a controller may be implemented as a proportional controller, where only a single parameter, Kc, is adjusted. Varying this gain results in a shift of the closed-loop poles across the complex plane. The root locus method provides a graphical means of tracking the movement of these poles as Kc varies, and constitutes the primary focus of this section.

Once the root locus has been determined, it becomes possible to identify two critical values: the ultimate gain (**Kcr**) and the ultimate period of oscillation (**Pcr**). With these values known, one can proceed to the systematic design of P, PI, and PID controllers using the Ziegler–Nichols tuning method. Additionally, the design of PI and PID controllers may also be carried out using the Tyreus–Luyben tuning method, which will be addressed in detail in the following section [10] [11].

Essentially, it is assumed that the controller employed in the system is a proportional (P) controller, characterized by the proportional gain Kc. The purpose of this assumption is to enable the construction of the root locus of the system, which in turn facilitates the determination of the ultimate gain Kcr and the ultimate period of oscillation Pcr.

The characteristic equation of the closed-loop system is given by:

$$G(s) = Gp(s) \cdot Gv(s) \cdot Gc(s) \cdot Gm(s) \quad \textbf{(3.1)}$$

where,

Gp(s): Transfer function of the process (plant)

$$Gp = \frac{6.4369 * 10^3}{5 * s \ + \ 1} \quad \textbf{(3.2)}$$

Gv(s): Transfer function of the actuator

$$Gv = \frac{1}{10 * s + 1} \quad \textbf{(3.3)}$$

Gc(s): Transfer function of the controller

$$Gc = Kc * (1 + \frac{1}{T_i s} + T_d s) \quad \textbf{(3.4)}$$

Gm(s): Transfer function of the measurement element (sensor)

$$Gm = \frac{1}{30 * s + 1} \tag{3.5}$$

This transfer function expression is used to compute the root locus, which graphically illustrates how the closed-loop poles migrate in the complex plane as the gain Kc varies.

Using MATLAB's computational tools, the root locus is plotted and visualized, typically as shown in a figure such as Figure 3.1. In this diagram, the horizontal axis corresponds to the real part of the complex frequency s, while the vertical axis represents the imaginary component. The position and movement of the poles in this plane provide direct insight into the stability and dynamic behavior of the system under varying control gain conditions.

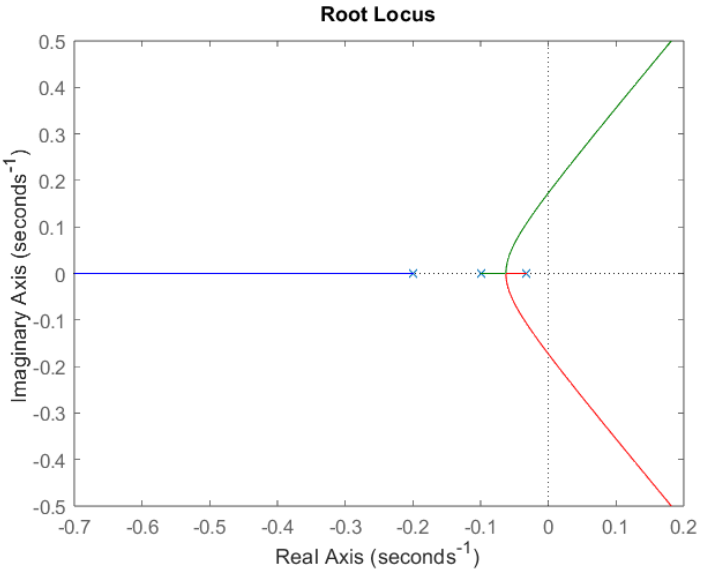

Figure 3.1: Root locus Analysis for H_2

It is evident that since the initial point of each root locus branch lies to the left of the imaginary axis—i.e., all system poles have negative real parts—the system under investigation is classified as **stable**.

From Figure 3.1, three distinct branches of the root locus are identified. The number of branches corresponds directly to the number of roots of the open-loop transfer function G(s), which in this case is n=3. The calculated poles of the system are located at: −0.2000, −0.1, and −0.0333. Which shows that the system is quite sensitive in model parameters.

Symmetry of the root locus with respect to the real axis is also observed, which is a typical property of root locus plots in linear time-invariant systems.

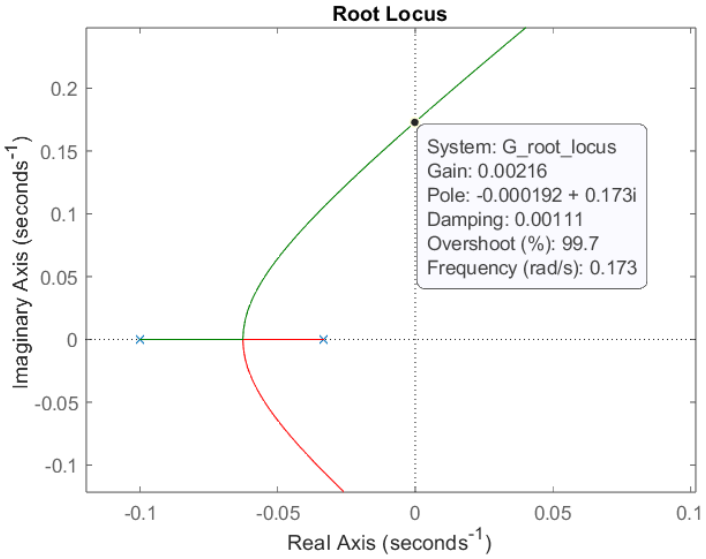

Figure 3.2: The intersection chosen point for H_2

From the information obtained in Figure 3.2, one can determine the key parameters required for this section, namely the critical Kcr and the critical oscillation period Pcr.

- $K_{cr} = \text{Gain} = 0.00216$
- $\text{Pole} = -0.000192 + 0.173 \cdot i$, $\omega = 0.173$ and $P_{cr} = \frac{2 \cdot \pi}{\omega} = 36.32$

3.2.2 Ziegler–Nichols Tuning Method and Tyreus–Luyben for Power Control

The method assumes that the system under control can be brought to the verge of instability by gradually increasing the proportional gain Kc, while keeping the integral and derivative actions deactivated. This leads to a condition where the system exhibits sustained oscillations. The gain at which this occurs is called the critical gain Kcr, and the period of the oscillations is the critical period Pcr.

Once Kcr and Pcr are identified—typically through root locus—these values are used to compute the controller parameters according to a predefined set of empirical formulas [9] [10].

Table 3.1: Ziegler-Nichols Setting in general form

Controller Type	K_c	τ_I	τ_D
P	$0.5 \cdot K_{cr}$	∞	0
PI	$0.45 \cdot K_{cr}$	$(\frac{1}{1.2}) \cdot P_{cr}$	0
PID	$0.6 \cdot K_{cr}$	$0.5 \cdot P_{cr}$	$0.125 \cdot P_{cr}$

where,

- Kc : Proportional gain
- τI : Integral time constant
- τD : Derivative time constant

Table 3.2: Ziegler-Nichols Setting in this system

Controller Type	K_c	τ_I	τ_D
P	0.0011	∞	0
PI	$9.72 * 10^{-4}$	30.27	0
PID	0.0013	18.16	4.54

The **Tyreus–Luyben** method is an empirical controller tuning approach developed as a refinement of the Ziegler–Nichols method, particularly suited for chemical process control systems and systems that require greater robustness and reduced oscillatory behavior.

This method also uses the ultimate gain (Kcr) and ultimate period (Pcr) obtained from the system's sustained oscillations under proportional-only control. However, compared to Ziegler–Nichols, Tyreus–Luyben tuning leads to less aggressive controller settings, enhancing stability margins and making it more appropriate for slower or integrating processes.

Table 3.3: Tyreus–Luyben Setting in general form

Controller Type	K_c	τ_I	τ_D
PI	$\frac{K_{cr}}{3.2}$	$2.2 \cdot P_{cr}$	0
PID	$\frac{K_{cr}}{2.2}$	$2.2 \cdot P_{cr}$	$\frac{P_{cr}}{6.3}$

Table 3.4: Tyreus–Luyben Setting in this system

Controller Type	K_c	τ_I	τ_D
PI	$6.75 * 10^{-4}$	79.90	0
PID	$9.82 * 10^{-4}$	79.90	5.76

3.2.3 Root Locus Analysis for Temperature

As in the previous section, in order to determine the key parameters required for controller tuning, the root locus method will once again be employed—this time focusing on the temperature control loop of the system. This analysis will be conducted in its simplest form, that is, assuming a proportional-only controller.

Through this approach, it becomes possible to identify two critical tuning parameters:

- The ultimate gain Kcr, which is the gain value at which the system begins to exhibit sustained oscillations
- The ultimate period of oscillation Pcr, corresponding to the period of these sustained oscillations

These two values will be used as the foundation for tuning PI and PID controllers using empirical methods such as Ziegler–Nichols or Tyreus–Luyben.

The characteristic equation of the closed-loop system will remain structurally identical to that used in the previous analysis (**Equation 3.1**). The only modification lies in the replacement of the transfer functions, which now correspond to the temperature control subsystem.

The transfer functions are the following:

Gp(s): Transfer function of the process (plant)

$$Gp = \frac{(0.3826 - 1.2307 * 10^{-4}) * (2515 * s + 8556) - 0.1429}{60.2599 * s^2 + 205.4189 * s + 1} \quad \textbf{(3.6)}$$

Gv(s): Transfer function of the actuator

$$Gv = \frac{1}{10 * s + 1} \quad \textbf{(3.7)}$$

Gc(s): Transfer function of the controller

$$Gc = Kc * (1 + \frac{1}{T_i s} + T_d s) \quad \textbf{(3.8)}$$

Gm(s): Transfer function of the measurement element (sensor)

$$Gm = \frac{1}{30 * s + 1} \quad \textbf{(3.9)}$$

Using MATLAB, the root locus method will be visually represented, allowing for a clear and intuitive analysis of how the closed-loop poles move in the complex plane as the controller gain Kc varies.

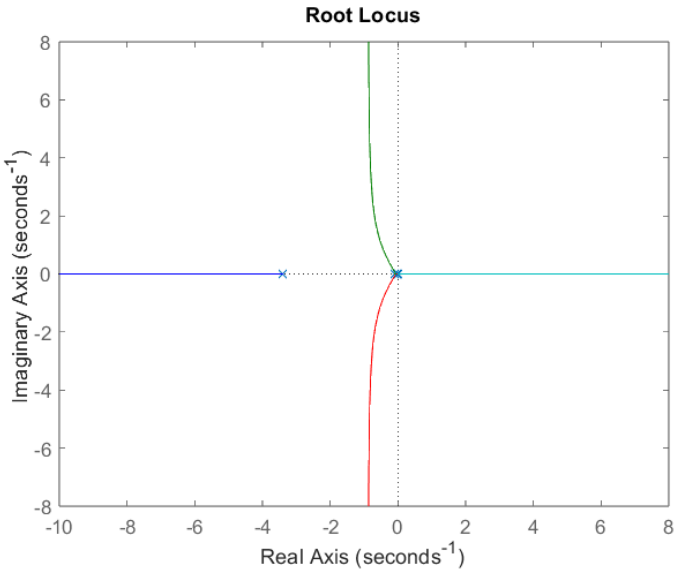

Figure 3.3: Root locus Analysis for Temperature

As shown in the figure above, since none of the root locus branches intersect the imaginary axis, it is not possible to directly determine the critical gain Kcr and the corresponding oscillation period Pcr from a standard crossing point.

Therefore, a representative point is arbitrarily selected along the cyan branch, as indicated in the plot. This selected point serves as a practical approximation to extract useful system behavior for controller tuning. While it does not represent the theoretical limit of marginal stability, it allows for the estimation of gain and oscillation characteristics that can still be used to design stable and responsive controllers, especially when applying empirical tuning rules such as those of Ziegler–Nichols or Tyreus–Luyben.

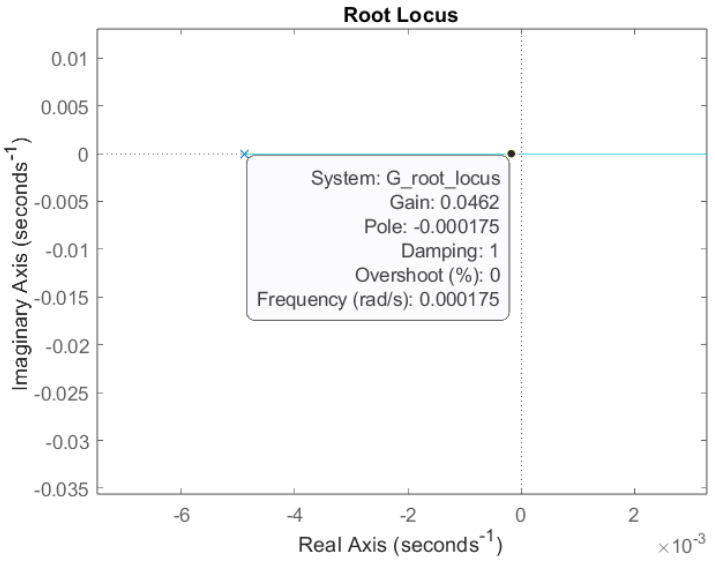

Figure 3.4: Root locus Analysis for Temperature

From the information obtained in Figure 3.2, one can determine the key parameters required for this section, namely the critical Kcr and the critical oscillation period Pcr.

- $K_{cr} = \text{Gain} = 0.0462$
- $\text{Pole} = -0.000175$

However, since the imaginary part ω cannot be zero—given that it is required to define an oscillatory response—we assign it a nominal value of 0.5 for the purposes of the continuation of this study.

This assumption allows us to approximate the oscillatory behavior of the system at the selected point on the root locus and proceed with the estimation of the critical oscillation period:

- $Pcr = \frac{2\pi}{\omega} = \frac{2\pi}{0.5} = 12.57$

3.2.4 Ziegler–Nichols Tuning Method and Tyreus–Luyben for Temperature Control

After determining the values of the critical gain Kcr and the critical oscillation period Pcr, the corresponding parameter tables for the Ziegler–Nichols tuning method are constructed below.

This method provides empirical formulas for calculating the proportional gain Kc, integral time Ti, and derivative time Td based on the values of Kcr and Pcr, with the goal of designing P, PI, and PID controllers

Table 3.5: Ziegler-Nichols Setting in this system

Controller Type	K_c	τ_I	τ_D
P	0.0231	∞	0
PI	0.0208	10.4750	0
PID	0.0277	6.285	1.5713

Next, the table corresponding to the Tyreus–Luyben tuning method is presented. This method, like Ziegler–Nichols, uses the critical gain Kcr and the critical period of oscillation Pcr, but provides more conservative tuning rules aimed at improving stability margins and reducing overshoot.

Below are the standard Tyreus–Luyben tuning formulas for PI and PID controllers:

Table 3.6: Tyreus–Luyben Setting in this system

Controller Type	K_c	τ_I	τ_D
PI	0.0144	27.6540	0
PID	0.021	27.6540	1.9952

3.3 Solution and Presentation of Diagrams of the P, PI, PID Controllers for Power Control

In the previous sections, five controllers were designed using the Ziegler–Nichols (P, PI, PID) and Tyreus–Luyben (PI, PID) tuning methods. These controllers are now to be implemented and simulated within the MATLAB environment to evaluate their performance [11].

The objective of this section is to carry out a series of simulations focusing on the hydrogen input–generated current output feedback control loop. Each of the five controllers will be applied to the same system, and their performance will be analyzed and compared based on their ability to drive the system to its desired steady-state value (set point). The selected controller will represent the most efficient and reliable choice for regulating the current output via hydrogen input in the PEM fuel cell control system.

The simulation begins with the implementation and evaluation of the **P (Proportional) controller**. As the simplest form of control, the P controller adjusts the control signal proportionally to the error between the system output and the desired set point. In this case, it acts on the hydrogen input flow to regulate the generated current. The exhibited overshoot is about 40A.

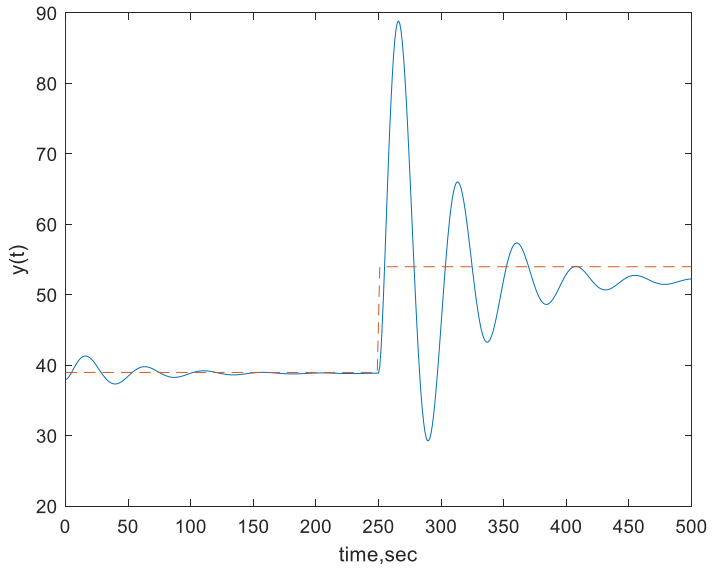

Figure 3.1: Output Response y(t)/ operating current in A of P (Proportional) controller Ziegler-Nichols

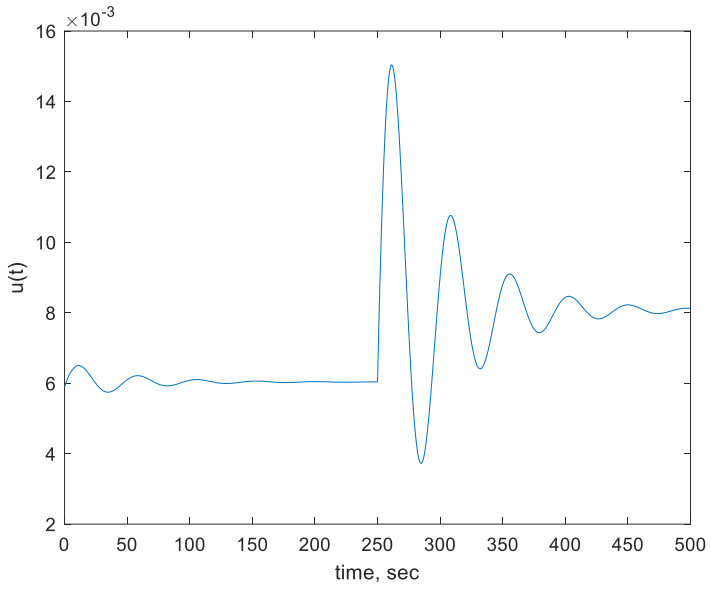

Figure 3.2: Input Response u(t)/ hydrogen flow rate in mol/s of P (Proportional) controller Ziegler-Nichols

As observed in the diagrams above, the performance of the P controller does not meet the desired specifications. Specifically, in Figure 3.1, the current response fluctuates around the set point but never actually reaches it. This behavior indicates that the system fails to stabilize at the target value, resulting in a persistent steady-state error. The proportional action alone is insufficient to fully eliminate the offset, which is a common limitation of P-only control. While the system demonstrates a degree of responsiveness, the absence of integral correction prevents it from converging precisely to the equilibrium point. Consequently, the P controller cannot adequately stabilize the system at the desired output level in this case. The presentation continues with the implementation of the **PI (Proportional–Integral) controller**. The exhibited overshoot is about 40A.

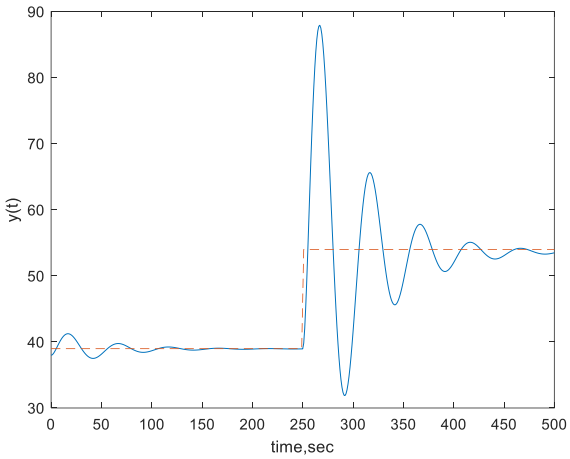

Figure 3.3: Output Response y(t)/ operating current in A of PI (Proportional-Integral) controller Ziegler-Nichols

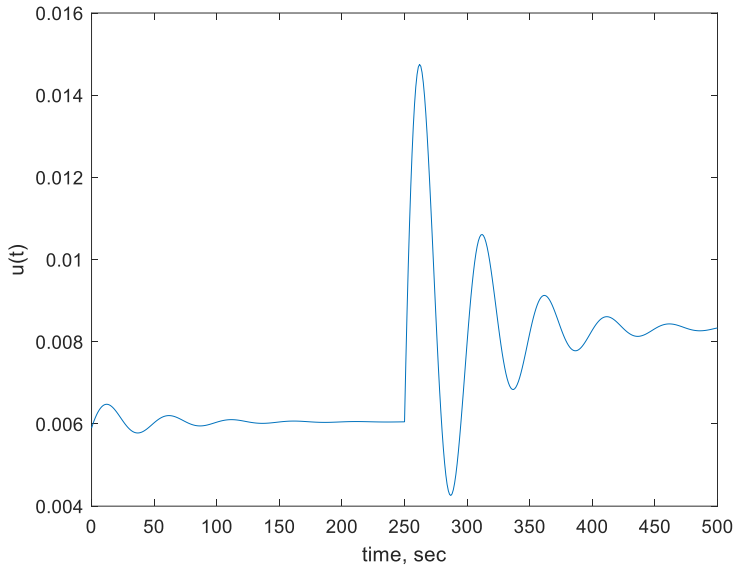

Figure 3.4: Input Response u(t)/ hydrogen flow rate in mol/s of PI (Proportional-Integral) controller Ziegler-Nichols

It is easy to observe the significant difference between the P and PI controllers. Initially, the PI controller reaches much closer to the desired set point which is 112A, exhibiting similar oscillatory behavior but with improved convergence.

The third controller in sequence is the **PID (Proportional–Integral–Derivative)** controller. This configuration combines the advantages of the previous controllers by integrating proportional, integral, and derivative actions into a single control law. The exhibited overshoot is about 50A.

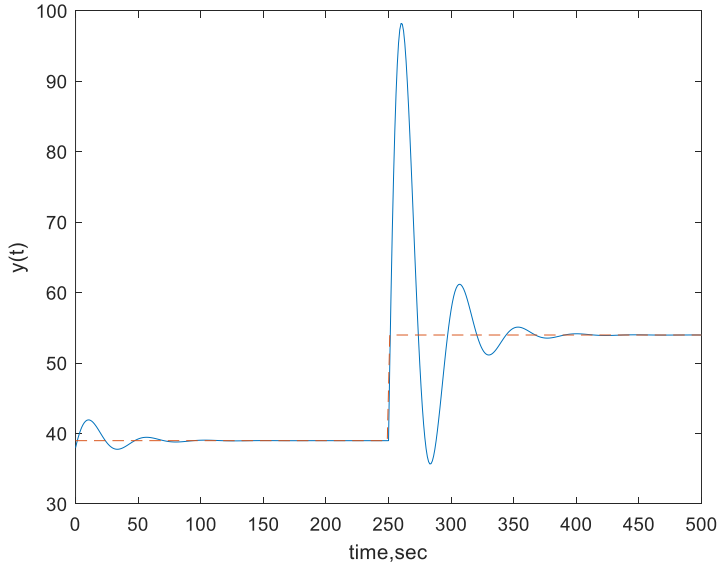

Figure 3.5: Output Response y(t)/ operating current in A of PID (Proportional–Integral–Derivative) controller Ziegler-Nichols

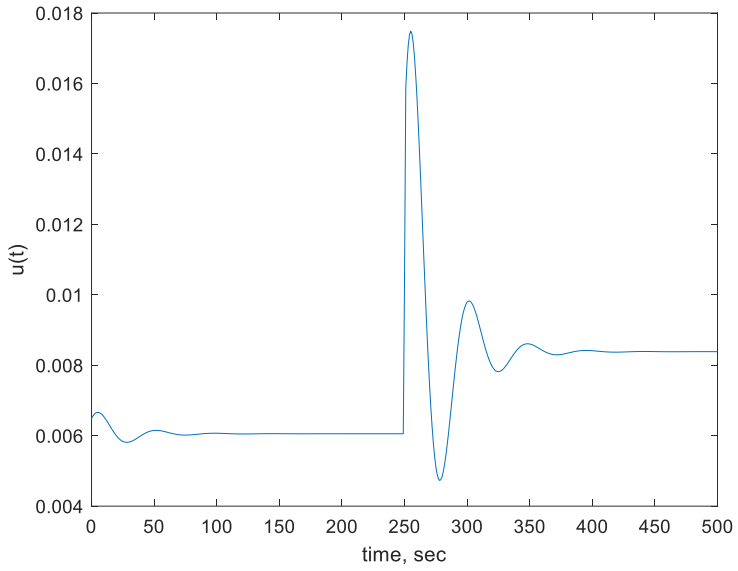

Figure 3.6: Input Response u(t)/ hydrogen flow rate in mol/s of PID (Proportional–Integral–Derivative) controller Ziegler-Nichols

As shown in Figure 3.5, the PID controller exhibits the most effective response compared to the previously examined controllers. It reaches the set point quickly and efficiently, demonstrating a significantly improved dynamic performance. More importantly, once the desired value is reached, the system maintains it with high precision and minimal deviation. The combined action of proportional, integral, and derivative terms enables the PID controller to minimize overshoot, eliminate steady-state error, and provide excellent stability. This results in a well-balanced and robust control response, confirming that the PID configuration offers the most accurate and reliable performance among the controllers analyzed so far. Following the presentation of the controllers tuned using the Ziegler–Nichols method, the analysis proceeds with the implementation of the **PI and PID controllers** designed according to **the Tyreus–Luyben method**. The exhibited overshoot is about 35A.

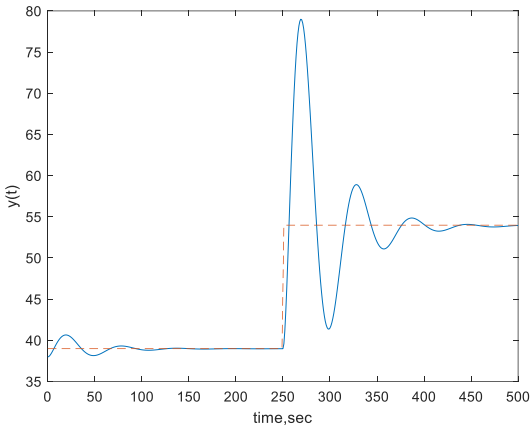

Figure 3.7: Output Response y(t)/ operating current in A of PI (Proportional–Integral) controller Tyreus–Luyben

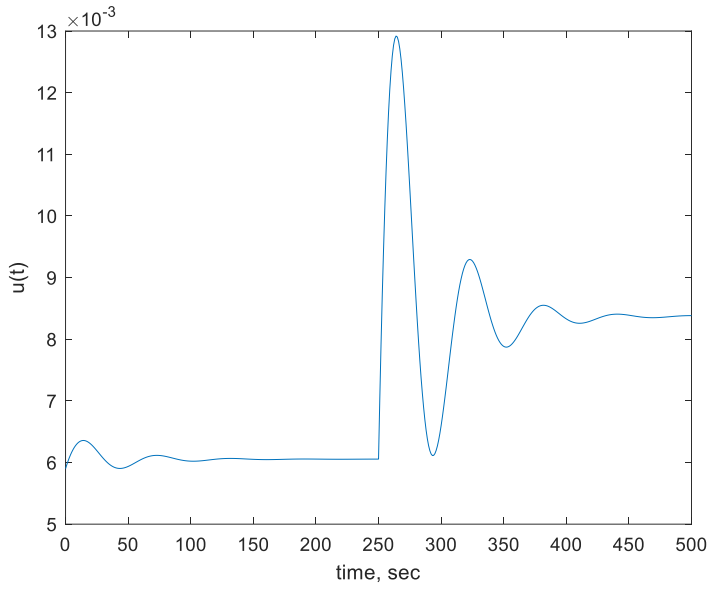

Figure 3.8: Input Response u(t)/ hydrogen flow rate in mol/s of PI (Proportional–Integral) controller Tyreus–Luyben

Regarding the results of the PI controller tuned using the Tyreus–Luyben method, several notable differences are observed when compared to the controller tuned with the Ziegler–Nichols method.

Firstly, the Tyreus–Luyben PI controller reaches the set point more quickly, and does so with significantly fewer oscillations. In addition, the amplitude of the fluctuations is substantially smaller, indicating improved damping characteristics. Importantly, the output does not drop below zero on the y-axis, suggesting enhanced stability and reduced overshoot.

Last but not least, the presentation concludes with the simulation of the **PID controller** tuned according to the **Tyreus–Luyben method**. The exhibited overshoot is about 33A.

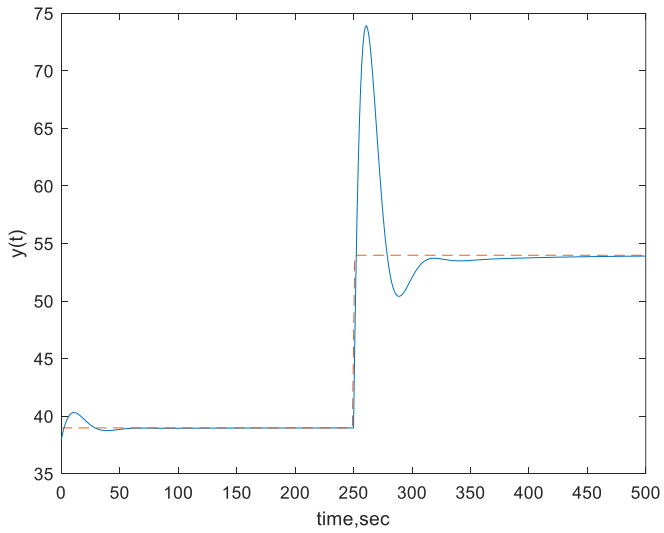

Figure 3.9: Output Response y(t)/ operating current in A of PID (Proportional–Integral–Derivative) controller Tyreus–Luyben

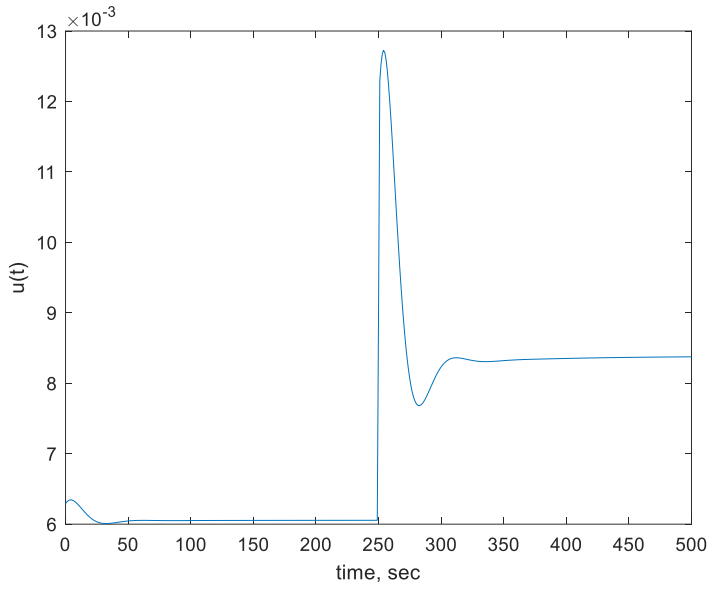

Figure 3.10: Input Response u(t)/ hydrogen flow rate in mol/s of PID (Proportional–Integral–Derivative) controller Tyreus–Luyben

In Figure 3.9, the control of the hydrogen inflow–generated current relationship, using a PID controller tuned via the Tyreus–Luyben method, demonstrates a very fast and efficient response. The system reaches the desired set point rapidly and without generating significant oscillations or overshoot. This behavior confirms the controller's ability to deliver a well-damped and stable performance, ensuring precise tracking of the reference value.

As a conclusion from the above analysis, it becomes evident that controlling the hydrogen flow in relation to the generated current can be a complex task, due to the dynamic behavior and sensitivity of the system. However, through the implementation of appropriately tuned controllers, it is possible to achieve a highly satisfactory performance in terms of both response speed and overall efficiency.

Among the controllers evaluated, the PID controllers—tuned using either the Ziegler–Nichols or Tyreus–Luyben methods—demonstrated the best results. Although both configurations performed effectively, the PID controller based on the Tyreus–Luyben method showed a slight advantage, primarily due to the reduced amplitude of oscillations during transient disturbances.

Table 3.7: Performance Criterion of Control

Performance Criterion	P_ZN	PI_ZN	PID_ZN	PI_TL	PID_TL
ISE	$3.795*10^3$	$3.133*10^3$	$1.896*10^3$	$2.980*10^3$	$1.798*10^3$
IAE	769.72	536.70	301.15	441.94	290.57
ITSE	$1.121*10^6$	$8.473*10^5$	$4.948*10^5$	$7.833*10^5$	$4.625*10^5$
IATE	$2.523*10^5$	$1.561*10^5$	$7.797*10^4$	$1.217*10^5$	$8.079*10^4$

Utot	3.592	3.646	3.693	3.653	3.6532
Ytot	$2.305*10^4$	$2.339*10^4$	$2.369*10^4$	$2.344*10^4$	$2.344*10^4$
Total_Energy	0.1924	0.195	0.1977	0.196	0.1956

The table above presents the various performance criteria used to quantitatively evaluate the efficiency and effectiveness of the controllers. These indices are based on the error signal e(t)=r(t)−y(t), where r(t) is the reference signal (set point) and y(t) is the system output. Each index captures a different aspect of the controller's behavior over time.

ISE (Integral of Squared Error):

$$ISE = \int_0^\infty e^2(t)\,dt$$

Emphasizes large errors more heavily. It is useful when penalizing large deviations is a priority.

IAE (Integral of Absolute Error):

$$IAE = \int_0^\infty |\,e(t)\,|\;dt$$

Penalizes total error over time equally, regardless of magnitude. It tends to produce smoother control actions.

ITSE (Integral of Time-weighted Squared Error):

$$ITSE = \int_0^\infty t \cdot e^2(t)\,dt$$

Places more weight on errors that persist over time. It helps reduce long-term error.

IATE (Integral of Time-weighted Absolute Error):

$$IATE = \int_0^\infty t \cdot |\,e(t)\,|\;dt$$

Similar to ITSE but gives linear weight to errors over time, focusing on sustained error reduction [24][26].

The PID controller with the Tyreus–Luyben method (consistently performs best in terms of error minimization, making it the most balanced and robust choice overall. The P_ZN controller is lowest in energy and effort, but its high error values indicate poor performance in precision-critical systems. It is also observed that the Utot (total control effort) values are relatively similar across all controllers, particularly among the PI and PID configurations, indicating that the control energy required does not significantly vary between these more advanced control strategies.

Finally, in terms of Total Energy, the controller associated with the highest energy output appears to be the PID_ZN.

More specific, from Table 3.7, two of the performance criteria select the PID controller tuned with the Ziegler–Nichols method, while the other two criteria favor the PID controller tuned using the Tyreus–Luyben method.

More specifically:

- The IATE and ISE criteria indicate better performance for the Ziegler–Nichols PID, suggesting slightly improved response in terms of accumulated absolute error over time and output magnitude.
- On the other hand, the ITSE and IAE metrics—both of which are widely considered primary indicators of tracking accuracy and error minimization—show superior performance for the Tyreus–Luyben PID, with lower error values and better damping behavior.

This balanced outcome highlights that while both PID controllers exhibit strong performance, the **Tyreus–Luyben PID** tends to provide more stable and accurate control, especially in systems where minimizing steady-state and transient error is critical.

3.4 Solutions and Presentation of Diagrams of the P, PI, PID Controllers in Temperature Control

In this section, the results concerning the temperature control of the system in relation to the coolant flow rate are presented. These results were obtained through simulations in MATLAB and aim to identify the most suitable controller for this specific subsystem.

The objective is to regulate the fuel cell's operating temperature by adjusting the coolant input, ensuring both thermal stability and dynamic performance. The process begins with the evaluation of the system's behavior under various control strategies, following the methodology used in the previous sections. The same tuning methods—Ziegler–Nichols and Tyreus–Luyben—will be applied, and their performance compared based on time-domain response, accuracy, and energy efficiency.

The analysis begins with the implementation of the **P (Proportional) controller**.

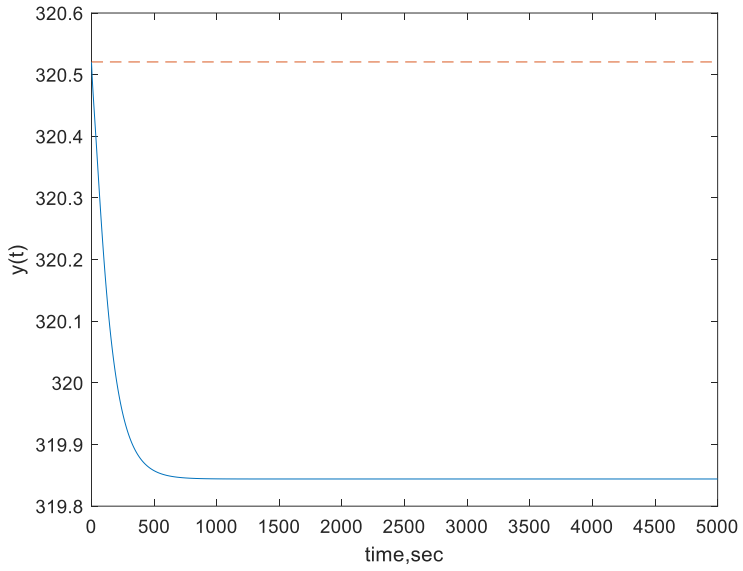

Figure 3.11: Output Response y(t)/ total temperature in K of P (Proportional) controller Ziegler-Nichols

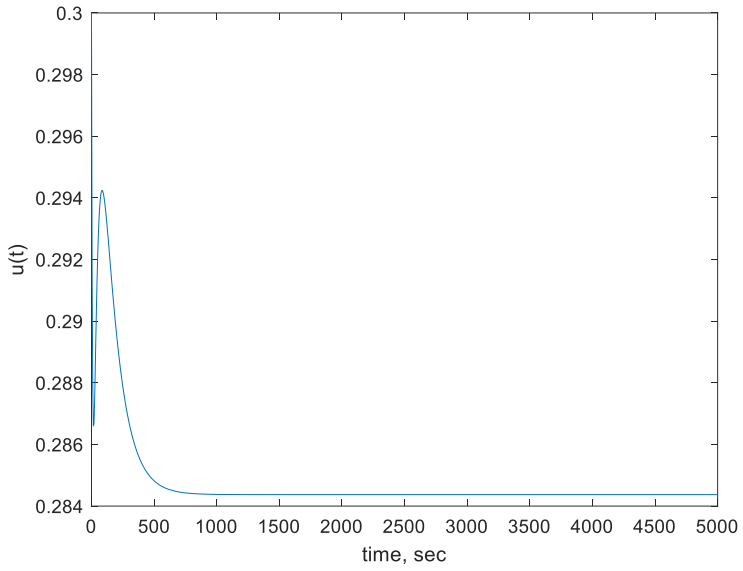

Figure 3.12: Input Response u(t)/ coolant flow rate in kg/s of P (Proportional) controller Ziegler-Nichols

As observed in the graphical representation of the P controller, the system initially reaches the desired temperature set point (approximately 322.55 K). However, this is followed by a noticeable decline, with the temperature eventually stabilizing slightly below 319 K. This behavior indicates that the proportional controller alone is insufficient for maintaining the output at the target value. The presentation continues with the implementation of the **PI (Proportional–Integral) controller**.

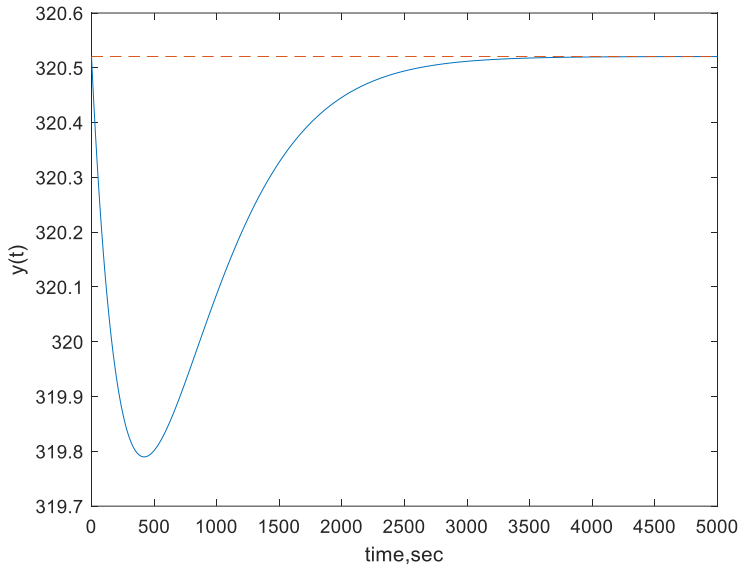

Figure 3.13: Output Response y(t)/ operating temperature in K of PI (Proportional–Integral) controller Ziegler-Nichols

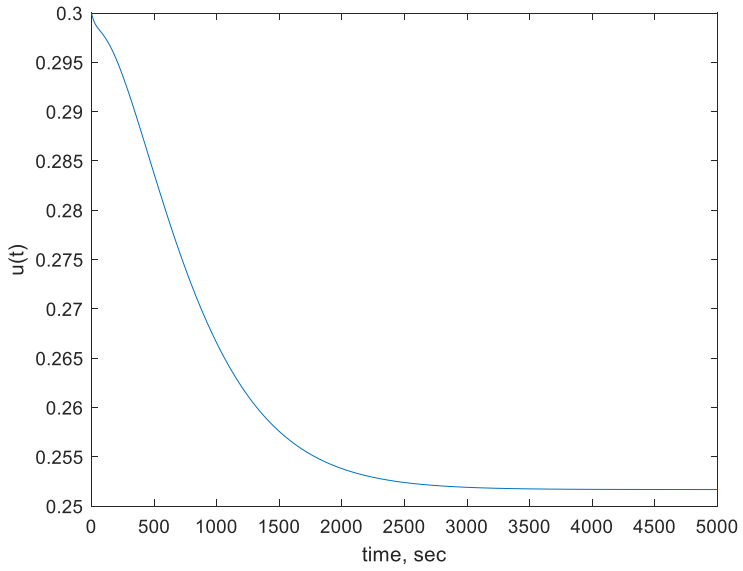

Figure 3.14: Input Response u(t)/ coolant flow rate in kg/s of PI (Proportional–Integral) Ziegler-Nichols

As illustrated in Figure 3.13, the response initially starts approximately at the set point. It is followed by a slight downward trend, after which the system rapidly recovers and converges smoothly to the desired temperature. This behavior indicates that the controller effectively corrects the initial deviation and ensures fast stabilization, achieving accurate set-point tracking with minimal overshoot.

The final controller presented using the Ziegler–Nichols tuning method is the **PID controller**.

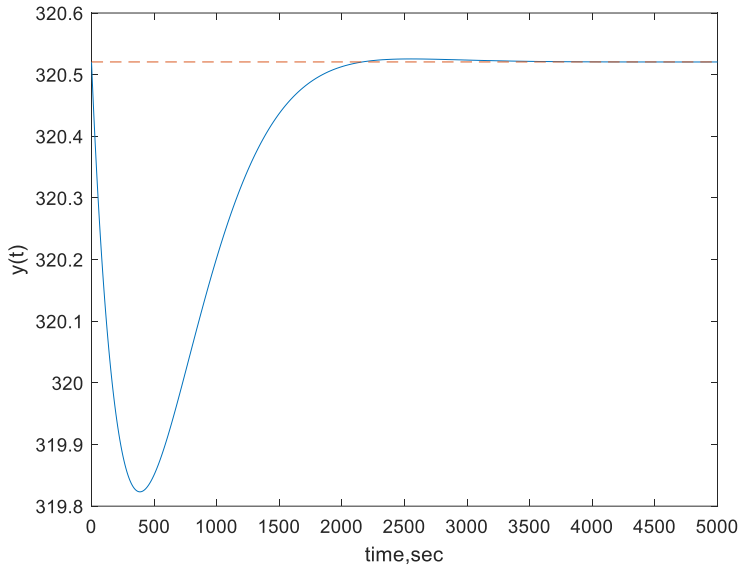

Figure 3.15: Output Response y(t)/ operating temperature in K of PID (Proportional–Integral–Derivative) controller Ziegler-Nichols

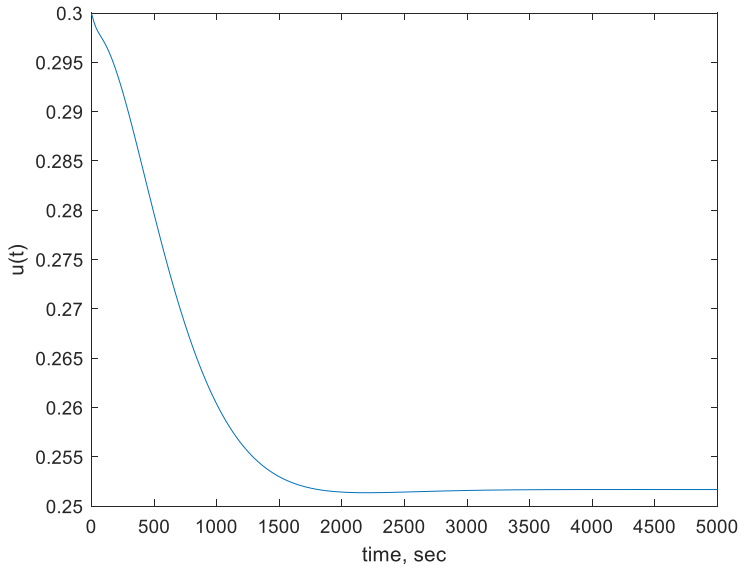

Figure 3.16: Input Response u(t)/ coolant flow rate in kg/s of PID (Proportional–Integral–Derivative) Ziegler-Nichols

In Figure 3.15, a similar response is observed with the application of the PI controller; however, the system exhibits a faster response and improved effectiveness. Specifically, the temperature reaches the desired set point of 322.55 K at a higher rate, demonstrating the superior dynamic performance of the PI controller in terms of both response time and accuracy.

The analysis now proceeds with the presentation of results obtained using the **PI controller with Tyreus–Luyben tuning method**.

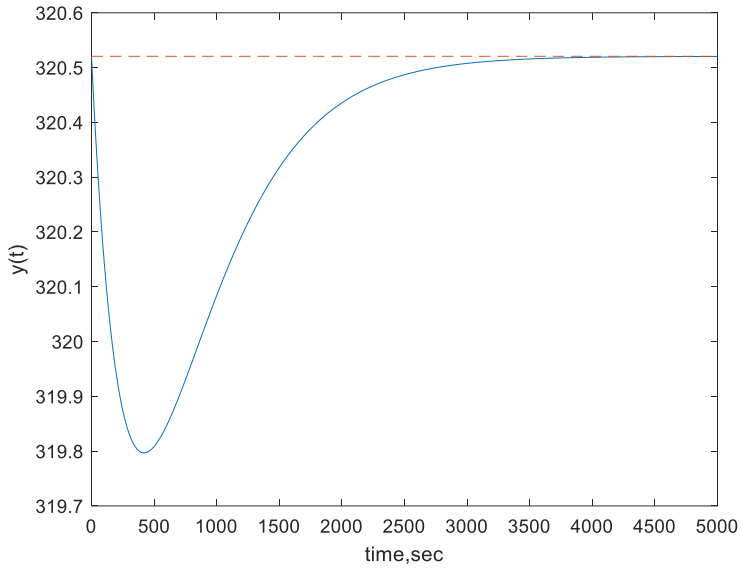

Figure 3.17: Output Response y(t)/ operating temperature in K of PI (Proportional–Integral) controller Tyreus–Luyben

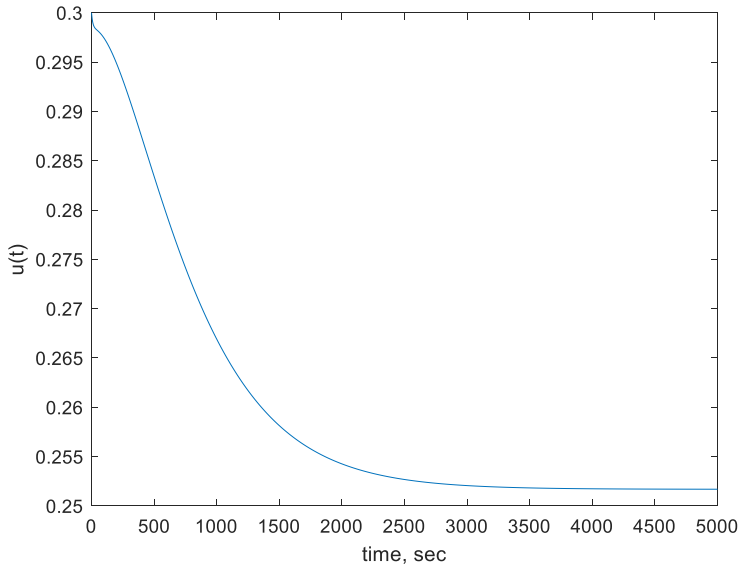

Figure 3.18: Input Response u(t)/ coolant flow rate in kg/s of PI (Proportional–Integral) controller Tyreus–Luyben

As illustrated above, the response curve of the PI controller closely resembles those of the two previous controllers, indicating that it is both rapid and effective in reaching the desired set point with relatively high speed.

The final controller examined in this analysis is the **PID controller tuned using the Tyreus–Luyben method**.

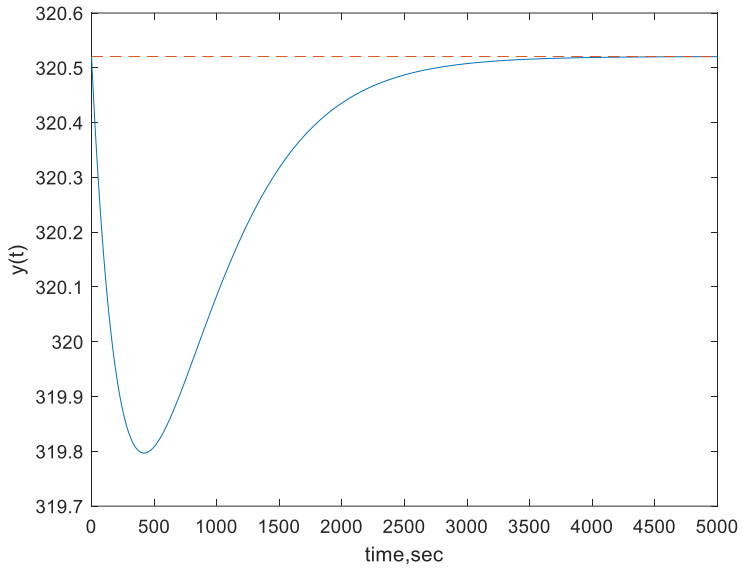

Figure 3.19: Output Response y(t)/ operating temperature in K of PID (Proportional–Integral–Derivative) controller Tyreus–Luyben

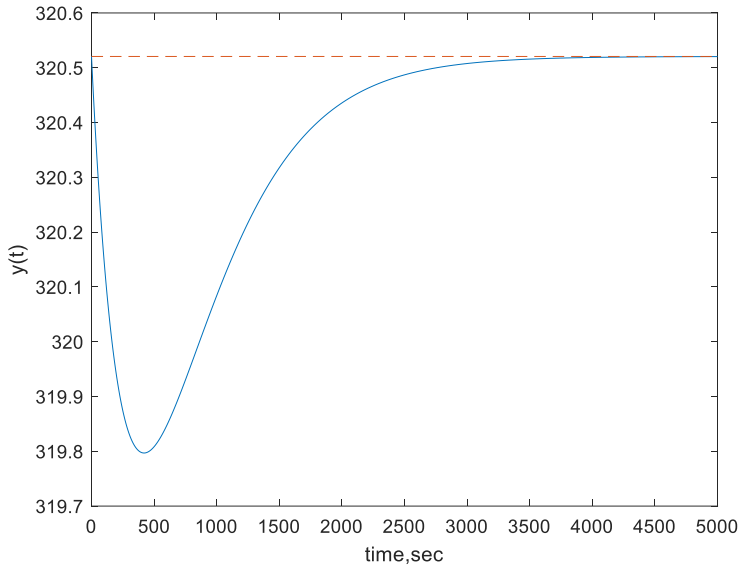

Figure 3.20: Input Response u(t)/ coolant flow rate in kg/s of PID (Proportional–Integral–Derivative) controller Tyreus–Luyben

Finally, as shown in Figure 3.19, the PID controller reaches the set point (322.55 K) with considerable speed and effectiveness, similarly to the three previously analyzed controllers.

Table 3.8: Performance Criterion of Control for Temperature

Performance Criterion	P_ZN	PI_ZN	PID_ZN	PI_TL	PID_TL
ISE	440.38	86.04	67.01	85.91	85.91
IAE	660.40	170.78	133.62	173.87	173.87
ITSE	$1.142*10^6$	$5.363*10^4$	$3.517*10^4$	$5.451*10^4$	$5.452*10^4$
IATE	$1.690*10^6$	$1.398*10^5$	$8.676*10^4$	$1.479*10^5$	$1.479*10^5$
Utot	15.21	40.41	42.29	40.26	40.26

The PID_ZN controller clearly dominates across all key performance criteria related to error minimization, including ISE, ITSE, and IATE, demonstrating its ability to provide both precise and stable temperature regulation. In contrast, the P_ZN controller achieves the lowest total control effort (Utot), which aligns with expectations for a proportional-only strategy. However, this lower actuation cost is offset by significantly higher error metrics, indicating poor tracking accuracy and inadequate control performance. Therefore, while P_ZN may be suitable in applications where control energy must be minimized and precision is not critical, for high-performance temperature control, PID_ZN offers the most effective balance between responsiveness, accuracy, and long-term stability.

In summary, while PI_TL demonstrates competitive performance in certain areas, especially in long-term error distribution, the **PID with Ziegler-Nichols** controller still delivers the best overall performance, striking the most effective balance between precision, responsiveness, and robustness in the temperature regulation of the system.

CONCLUSIONS

This thesis focused on the dynamic modeling, linearization, and control of a Proton Exchange Membrane (PEM) fuel cell stack, aiming to analyze its behavior and optimize its performance through the implementation of appropriate control strategies.

In Chapter 1, a nonlinear mathematical model of the system was developed, based on differential equations that describe the electrochemical, thermal, and mass dynamics of the fuel cell stack. The model was then linearized using a Taylor series expansion around selected steady-state operating points. The resulting linear model was transformed into state-space representation, enabling further analysis and the application of advanced control techniques.

In Chapter 2, simulations were carried out using MATLAB to solve the three models developed in Chapter 1: the nonlinear model, the linearized model, and the state-space model. The graphical results demonstrated that all three models produce consistent outcomes, validating the reliability and repeatability of the state-space model. To further verify the consistency of the models, a series of simulations was conducted under altered initial conditions, introducing ±30% variations in the hydrogen input flow rate (Fin_H2) and the coolant mass flow rate (mcool). These sensitivity tests confirmed that all models maintained accurate and comparable behavior under dynamic scenarios.

Chapter 3, the most critical part of the thesis, focused on the design and evaluation of control systems. It began with a theoretical discussion on feedback control, emphasizing the root locus method to identify the system poles and extract the critical parameters Kcr and Pcr. Based on these parameters, P, PI, and PID controllers were tuned using both the Ziegler–Nichols and Tyreus–Luyben methods. The control strategies were applied to two key subsystems:

- The output current (Ifc) with respect to the hydrogen input flow (Fin_H2), and
- The output temperature (Tout) with respect to the coolant flow rate (mcool).

The performance of each controller was assessed using several standard performance indices, including ISE, IAE, ITSE, IATE, and total control effort (Utot). The results showed that for current control, the **PID controller tuned via Tyreus–Luyben** demonstrated the best performance, offering a balance of responsiveness and minimal oscillations. For temperature regulation, the **PID controller using Ziegler–Nichols** was marginally superior, primarily due to its faster convergence to the set point and stable behavior.

In conclusion, this thesis demonstrated that precise mathematical modeling, combined with appropriate controller design and tuning, is essential for the efficient operation of PEM fuel cell stacks, especially in high-performance applications such as vehicle propulsion. The methodologies and analyses presented form a robust framework for understanding, simulating, and controlling PEM fuel cell systems and offer a solid foundation for future research and optimization.

BIBLIOGRAPHY

1. Akshay Kumar Rathore, P. U. (2011). *Novel Snubberless Bidirectional ZCS/ZVS Current-Fed Half-Bridge Isolated Dc/Dc Converter for Fuel Cell Vehicles.*

2. Barbir, F. (2012). *PEM FUEL CELLS THEORY AND PRACTICE.*

3. James Larminie, A. D. (2003). *Fuel Cell Systems Explained: Second Edition.*

4. Ridden, P. (2011). PowerTrekk fuel cell allows for power on the go. *NEW ATLAS.*

5. Tabbi Wilberforce Awotwe, A. A. (2016). *ADVANCES IN STATIONARY AND PORTABLE FUEL CELL APPLICATIONS.*

6. W.R.W Daud, R. R. (2017). *PEM fuel cell system control: A review.*

7. Βελώνη, Α. (2013). Ψηφιακά Σ.Α.Ε: Περιγραφή στο Χώρο – Κατάστασης. Στο Α. Βελώνη, *Συστήματα Αυτόματου Ελέγχου.*

8. Δαπόντης, Σ. (2024). *Σχεδιασμός και προσομοίωση ενός αποκεντρωμένου συστήματος ελέγχου για Μονάδα Ηλεκτρόλυσης τύπου PEM.* ΠΟΛΥΤΕΧΝΕΙΟ ΚΡΗΤΗΣ, ΜΠΔ. ΧΑΝΙΑ: ΠΟΛΥΤΕΧΝΕΙΟ ΚΡΗΤΗΣ. Ανάκτηση από https://dias.library.tuc.gr/view/100380

9. Δημήτρης, Ιψάκης (2023). *Σύστημα Ελέγχου με Ανατροφοδότηση & (Δομικά) Διαγράμματα Βαθμίδων.* ΧΑΝΙΑ: ΠΟΛΥΤΕΧΝΕΙΟ ΚΡΗΤΗΣ.

10. Δημήτρης, Ιψάκης (2025). *Σχεδιασμός ή Σύνθεση Ελεγκτών με Ανάδραση.* ΧΑΝΙΑ: ΠΟΛΥΤΕΧΝΕΙΟ ΚΡΗΤΗΣ.

11. Ελευθερίου, Σ. (2023). *Εφαρμογή και σύγκριση μεθόδων συντονισμού παραμέτρων ενός PID ελεγκτή.* ΠΟΛΥΤΕΧΝΕΙΟ ΚΡΗΤΗΣ, ΜΠΔ. ΧΑΝΙΑ: ΠΟΛΥΤΕΧΝΕΙΟ ΚΡΗΤΗΣ. Ανάκτηση από https://dias.library.tuc.gr/view/96654

12. Ευτυχία, Μ. (2015). *Ανάλυση Λειτουργίας Κυψελών Καυσίμου και Μοντελοποίηση τους με τη Χρήση του Λογισμικού Simulink.* ΧΑΝΙΑ: ΠΟΛΥΤΕΧΝΕΙΟ ΚΡΗΤΗΣ.

13. Ζιώγου, Χ. Ο. (2009). *Ρύθμιση συστήματος κυψέλης καυσίμου βασισμένη σε μαθηματικό μοντέλο προβλεπτικού ελέγχου (predictive) και ανίχνευση βέλτιστου σημείου λειτουργίας.* ΘΕΣΣΑΛΟΝΙΚΗ.

14. Ζουντουρίδου, Ε. Ι. (2006). *ΑΝΑΛΥΣΗ – ΛΕΙΤΟΥΡΓΙΑ ΚΥΨΕΛΩΝ ΚΑΥΣΙΜΟΥ ΚΑΙ ΠΡΟΣΟΜΟΙΩΣΗ ΛΕΙΤΟΥΡΓΙΑΣ ΚΥΨΕΛΗΣ ΚΑΥΣΙΜΟΥ ΜΕΜΒΡΑΝΗΣ ΑΝΤΑΛΛΑΓΗΣ ΠΡΩΤΟΝΙΩΝ (PEMFC) ΓΙΑ ΤΗΝ ΠΑΡΑΓΩΓΗ ΗΛΕΚΤΡΙΚΗΣ ΕΝΕΡΓΕΙΑΣ.* ΑΘΗΝΑ.

15. Ιψάκης, Δ. (2011). *ΣΧΕΔΙΑΣΜΟΣ ΒΕΛΤΙΣΤΗΣ ΛΕΙΤΟΥΡΓΙΑΣ ΕΝΕΡΓΕΙΑΚΩΝ ΣΥΣΤΗΜΑΤΩΝ ΜΕ ΧΡΗΣΗ ΑΝΑΝΕΩΣΙΜΩΝ ΚΑΙ ΕΝΑΛΛΑΚΤΙΚΩΝ ΠΗΓΩΝ.* ΘΕΣΣΑΛΟΝΙΚΗ.

16. Κοντογιάννης, Θ. (2024). *ΜΟΝΤΕΛΟΠΟΙΗΣΗ ΚΑΙ ΠΡΟΣΟΜΟΙΩΣΗ ΚΥΨΕΛΗΣ ΚΑΥΣΙΜΟΥ ΤΥΠΟΥ PEM.* ΠΟΛΥΤΕΧΝΕΙΟ ΚΡΗΤΗΣ, ΜΠΔ. ΧΑΝΙΑ: ΠΟΛΥΤΕΧΝΕΙΟ ΚΡΗΤΗΣ. Ανάκτηση από https://dias.library.tuc.gr/view/98755

17. Κουτσούμπας, Λ. (2021). *Ανάπτυξη συστήματος ελέγχου κυψέλης καυσίμου για ηλεκτρικά οχήματα.* ΧΑΝΙΑ: ΠΟΛΥΤΕΧΝΕΙΟ ΚΡΗΤΗΣ.

18. Λυμπεροπούλου, Χ. (2017). *Μοντελοποίηση Κυψέλης Καυσίμου.*

19. Μαρνέλλος, Γ. (2013). Κυψέλες Καυσίμου. Στο Γ. Μαρνέλλος, *Ειδικά Κεφάλαια Παραγωγής Ενέργειας.*

20. Μπούταλης, Ι. (χ.χ.). *Συστήματα αυτόματου ελέγχου (ΙΙ) Modern Control Theory.*

21. Τσαπατσούλης, Ν. (2006). *Ανάλυση Σ.Α.Ε στο χώρο κατάστασης.*

22. Matlab Documentation, https://www.mathworks.com/help/control/ug/transfer-functions.html, Accessed on 30/06/2025

23. https://www.electronics-tutorials.ws/systems/closed-loop-system.html Accessed on 04/04/2025

24. https://www.scribd.com/document/507764040/04-Performance-Criteria Accessed on 14/05/2025

25. https://www.slideshare.net/meenasundar/class-32-performance-criteria-for-tuning-controllers Accessed on 14/06/2025

26. Green Car Congress: ICCT LCA study finds only battery and hydrogen fuel cell EVs have potential to be very low-GHG passenger vehicle pathways, 21 July 2021

27. Fuel Cell Types. Source: E4Tech, FUEL CELL INDUSTRY REVIEW, 2016.

APPENDIX

The following section presents in detail the equations corresponding to the state variables used for the construction of the state-space matrices described in Section 1.3. Each equation is accompanied by the respective notation, as defined in the reference table.

$$a1 = \frac{1}{m_{fc}*Cp_{fc}} * ((-(Cp_{fc_{WATER}} - 0.5 * Cp_{fc_{OXYGEN}} - Cp_{fc_{HYDROGEN}}) * ((nc * Ifcss)/(ne * Far)) * nf) - (Ufc * Afc * nc) - 4 * sig * Afc * nc * ((Tout_{fc\_ss})\text{^}3)) \quad \textbf{(2.1)}$$

$$a6 = \frac{1}{m_{fc}*Cp_{fc}} * (Ufc * Afc * nc) \quad \textbf{(2.2)}$$

$$a8 = \frac{1}{m_{fc} * Cp_{fc}} * (-((DH_{WATER\_o} - 0.5 * DH_{OXYGEN\_o} - DH_{HYDROGEN\_o}) + (Cp_{fc_{WATER}} - 0.5 * Cp_{fc_{OXYGEN}} - Cp_{fc_{HYDROGEN}}) * (Tout_{fc\_ss} - Tref)) * ((nc)/(ne * Far) * n\_f) + nc * (1.253 - Vfc)) \quad \textbf{(2.3)}$$

$$b1 = \frac{1}{V_{anode}} * (\frac{-F_{out_{fc_{hydrogen_{an_{ss}}}}} * Rg}{Pfc*10^5} * C_{out\_fc\_hydrogen\_an\_ss}) \quad \textbf{(2.4)}$$

$$b2 = \frac{1}{V_{anode}} * (\frac{-F_{out_{fc_{hydrogen_{an_{ss}}}}} * Rg * Tout_{fc_{ss}}}{Pfc*10^5}) \quad \textbf{(2.5)}$$

$$b8 = \frac{1}{V_{anode}} * (-\frac{nc}{ne*Far} * nf) \quad \textbf{(2.6)}$$

$$b10 = \frac{1}{V_{anode}} * (-\frac{Rg*Tout_{fc\_ss}}{Pfc*10^5}) * C_{out\_fc\_hydrogen\_an\_ss} \quad \textbf{(2.7)}$$

$$c1 = \frac{1}{V_{cathode}} * (-\frac{F_{out_{fc_{oxygen_{cat_{ss}}}}} + F_{out_{fc_{nitrogen_{cat_{ss}}}}}) * Rg}{Pfc*10^5}) * Cout\_fc\_oxygen\_cat\_ss \quad \textbf{(2.8)}$$

$$c3 = \frac{1}{V_{cathode}} * (-(F_{out_{fc_{oxygen_{cat_{ss}}}}} + F_{out_{fc_{nitrogen_{cat_{ss}}}}}) * Rg * \frac{Tout_{fc_{ss}}}{Pfc * 10^5}) \quad \textbf{(2.9)}$$

$$c8 = \frac{1}{V_{cathode}} * (-0.5 * \frac{nc}{ne*Far} * nf) \quad \textbf{(2.10)}$$

$$c11 = \frac{1}{V_{cathode}} * (-\frac{Rg*Tout\_fc\_ss}{Pfc*10^5} * C_{out\_fc\_oxygen\_cat\_ss}) \quad \textbf{(2.11)}$$

$$c12 = \frac{1}{V_{cathode}} * (-\frac{Rg*Tout\_fc\_ss}{Pfc*10^5} * C_{out\_fc\_oxygen\_cat\_ss}) \quad \textbf{(2.12)}$$

$$d1 = \frac{1}{V_{cathode}} * \left(\frac{-(F_{out_{fc_{oxygen_{cat_{ss}}}}} + F_{out_{fc_{nitrogen_{cat_{ss}}}}}) * Rg}{Pfc * 10^5} * C_{out\_fc\_nitrogen\_cat\_ss}\right) \quad \textbf{(2.13)}$$

$$d4 = \frac{1}{V_{cathode}} * \frac{(-(F_{out_{fc_{oxygen_{cat_{ss}}}}} + F_{out_{fc_{nitrogen_{cat_{ss}}}}}) * Rg * Tout_{fc_{ss}})}{Pfc * 10^5} \quad \textbf{(2.14)}$$

$$d11 = \frac{1}{V_{cathode}} * \left(-\frac{Rg * Tout\_fc\_ss}{Pfc * 10^5} * C_{out\_fc\_nitrogen\_cat\_ss}\right) \quad \textbf{(2.15)}$$

$$d12 = \frac{1}{V_{cathode}} * \left(-\frac{Rg * Tout\_fc\_ss}{Pfc * 10^5} * C_{out\_fc\_nitrogen\_cat\_ss}\right) \quad \textbf{(2.16)}$$

$$e5 = \frac{1}{V_{cathode}} * (-(18 * 10^{-6}) * F_{out\_fc\_water\_cat\_ss}) \quad \textbf{(2.17)}$$

$$e8 = \frac{1}{V_{cathode}} * \left(\frac{nc}{ne * Far} * nf\right) \quad \textbf{(2.18)}$$

$$e13 = \frac{1}{V_{cathode}} * (-(18 * 10^{-6}) * C_{out\_fc\_water\_cat\_ss}) \quad \textbf{(2.19)}$$

$$f1 = \left(\frac{1}{p_{cool\_fc} * V_{cool\_fc} * cp_{cool\_fc}}\right) * (Ufc * Afc * nc) \quad \textbf{(2.20)}$$

$$f6 = \left(\frac{1}{p_{cool\_fc} * V_{cool\_fc} * cp_{cool\_fc}}\right) * (-m_{cool\_fc} * cp_{cool\_fc} - Ufc * Afc * nc) \quad \textbf{(2.21)}$$

$$g8 = -\frac{1}{t\_fc} \quad \textbf{(2.22)}$$

$$h8 = \frac{V\_total}{t\_fc} \quad \textbf{(2.23)}$$

$$h9 = \frac{-1}{t\_fc} \quad \textbf{(2.24)}$$

$$i8 = \frac{1}{4} * \left(-\frac{nc}{ne * Far} * nf\right) \quad \textbf{(2.25)}$$

$$i10 = -\frac{1}{4} \quad \textbf{(2.26)}$$

$$j8 = \frac{1}{4} * \left(-\frac{0{,}5 * nc}{ne * Far} * nf\right) \quad \textbf{(2.27)}$$

$$j11 = -\frac{1}{4} \quad \textbf{(2.28)}$$

$$k12 = -\frac{1}{4} \quad \textbf{(2.29)}$$

$$l8 = \frac{1}{4} * \left(-\frac{nc}{ne * Far} * nf\right) \quad \textbf{(2.30)}$$

$$l13 = (1/4) * (-1) \quad \textbf{(2.31)}$$

$$s8 = 0.53 \quad \textbf{(2.32)}$$

$$s19 = -1 \quad \textbf{(2.33)}$$

$$ba6 = \frac{1}{m_{fc} * Cp_{fc}} * (Cp_{fc_{WATER}} - 0.5 * Cp_{fc_{OXYGEN}} - Cp_{fc_{HYDROGEN}}) * (\frac{nc}{ne * Far} * nf) \quad \textbf{(2.34)}$$

$$bb1 = \frac{1}{V_{anode}} \quad \textbf{(2.35)}$$

$$bc1 = \frac{1}{V_{cathode}} * O\_H \quad \textbf{(2.36)}$$

$$bd1 = \frac{1}{V_{cathode}} * O\_H * \frac{79}{21} \quad \textbf{(2.37)}$$

$$bh1 = (Ut\_factor * (\frac{\frac{ne * Far * n\_f}{nc}}{t\_fc}) \quad \textbf{(2.38)}$$

$$bj1 = \frac{1}{4} \quad \textbf{(2.39)}$$

$$bk2 = \frac{1}{4} * O\_H \quad \textbf{(2.40)}$$

$$bl3 = \frac{1}{4} * O_H * \frac{79}{21} \quad \textbf{(2.41)}$$

$$bf2 = cp_{cool_{fc}} * \frac{T_{cool\_in_{fc\_ss}} - T_{cool_{fc\_ss}}}{pcool_{fc} * Vcool_{fc} * cp_{cool_{fc}}} \quad \textbf{(2.42)}$$

$$bf3 = \frac{mcool_{fc\_ss} * cp_{cool_{fc}}}{pcool_{fc} * Vcool_{fc} * cp_{cool_{fc}}} \quad \textbf{(2.43)}$$